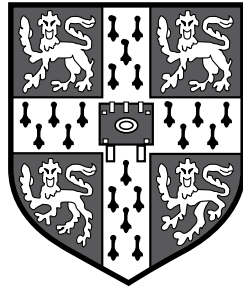


Inverse problems in haemodynamics and magnetic resonance velocimetry



UNIVERSITY OF
CAMBRIDGE

Alexandros Kontogiannis

Matthew Juniper (Supervisor)

Luca Magri (Adviser)

Department of Engineering
University of Cambridge

Preliminary examination for the degree of
Doctor of Philosophy

Abstract

Patient-specific cardiovascular modeling relies on the proper formulation of an inverse problem. This problem combines theoretical and experimental knowledge to provide insight to ‘hidden’, or uncertain, physiologically relevant model parameters. In this report, we study inverse problems that combine a magnetic resonance velocimetry (MRV) signal with a physical model describing fluid motion. Given a MRV image, we derive an algorithm that infers the most likely boundaries of the flow, the boundary conditions, the kinematic viscosity, and the body forces. We do this by minimizing a discrepancy norm of the velocity fields between the MRV experiment and the theoretical model, and add regularization terms to mitigate the ill-posedness of the problem. The inferred model parameters are subsequently used to revise the physical model, rendering it quantitatively accurate. At the same time, we obtain a denoised and higher-resolution (reconstructed) version of the original MRV signal. We test the algorithm for flows governed by a Poisson or a Stokes problem, using both real and synthetic MRV measurements, and discuss the potential use of the above methods in medical diagnosis and MRV signal reconstruction.

Table of contents

Nomenclature	vii
1 Introduction	1
1.1 Fluid mechanics of large blood vessels	1
1.2 Principles of magnetic resonance imaging/velocimetry	3
1.3 Inverse problems in cardiovascular fluid mechanics	4
1.4 Conclusions and Research objectives	7
2 Reconstruction of unknown quantities	9
2.1 Shape of the object	9
2.1.1 Shape inference using the Poisson equation	9
2.1.2 Extension to the Stokes problem	22
2.2 Viscosity, forcing and boundary conditions	31
2.2.1 Euler-Lagrange equations	31
2.2.2 Regularization	32
2.2.3 Two problems with multiple unknowns	34
3 Conclusions and future work	39
References	43
Appendix A Shape sensitivity analysis	49

Nomenclature

Symbols

\mathbf{u}, u	flow velocity, and velocity magnitude
\mathbf{u}^*, u^*	experimental measurement of flow velocity, and velocity magnitude
p	pressure
$\boldsymbol{\tau}_w$	wall shear stress tensor
\mathbf{f}	force exerted on the fluid (forcing term)
\mathbf{g}	term of non-homogeneous Neumann boundary condition
\mathbf{g}^*	ground truth of \mathbf{g}
μ	dynamic viscosity
ν	kinematic viscosity or normal vector (when not to be confused)
$\boldsymbol{\nu}$	normal vector
$\hat{\boldsymbol{\nu}}$	extension of the normal vector of $\partial\Omega$ to I
Ω	domain of solution for a boundary value problem (or blood vessel geometry)
$\bar{\Omega}$	closure of Ω , or $\Omega \cup \partial\Omega$
Ω^*	ground truth of Ω
$\partial\Omega$	($\equiv \partial\Omega^+$) boundary of Ω with an outward facing normal vector
$\partial\Omega^-$	boundary of Ω with an inward facing normal vector
Γ	subset of the boundary of Ω corresponding to the ‘walls’
Γ_i	subset of the boundary of Ω corresponding to the ‘inlet’
Γ_o	subset of the boundary of Ω corresponding to the ‘outlet’
I	whole domain, regarded as the image in which Ω is embedded, or the identity operator

ϕ_{\pm}	signed distance function of Ω
\mathcal{V}	speed field of the moving domain Ω (vector)
\mathcal{V}^*	optimal speed field (shape gradient) \mathcal{V}
$\overset{\circ}{\mathcal{V}}$	extension of \mathcal{V} from $\partial\Omega$ to I
ζ	magnitude of speed field (scalar)
ζ^*	magnitude of shape gradient
$\overset{\circ}{\zeta}$	extension of ζ from $\partial\Omega$ to I
δ	Dirac measure
h	mesh size
\mathcal{J}	discrepancy (or error) functional
\mathcal{R}	regularization term of an inverse problem
\mathcal{N}	Nitsche terms for the weak enforcement of boundary conditions
\mathcal{S}	sampling pattern operator (measurement operator)
\mathcal{C}	covariance operator
\mathbb{E}	expectation operator
u'	shape derivative of u due to \mathcal{V}
$D_{\mathcal{V}}$	($\equiv u' + (\mathcal{V} \cdot \nabla)u$) material derivative of u along \mathcal{V}
∂_{ν}	($\equiv \nu \cdot \nabla$) normal derivative operator
\mathcal{F}	Fourier transform
\hat{u}	($\equiv \mathcal{F}u$) Fourier transform of u
$\mathcal{N}(m, \mathcal{C})$	Gaussian measure with mean m and covariance operator \mathcal{C}
$\text{sgn}()$	sign function
$A \Subset B$	A is compactly contained in B , i.e. ‘there is always space between A and B ’
$A \setminus B$	set A minus set B , or $A \cap B^c$ with B^c the complement of B

Function spaces, norms, and inner products

$C^k(\Omega)$	space of k -continuously differentiable functions in Ω
$\mathcal{D}(\Omega)$	($\equiv C_c^{\infty}(\Omega)$) space of smooth functions with compact support in Ω

$\mathcal{D}'(\Omega)$	space of distributions (generalized functions) in Ω (dual of $\mathcal{D}(\Omega)$)
$H^k(\Omega)$	space of square-integrable functions in Ω with k square-integrable derivatives
$H_0^1(\Omega)$	H^1 space of functions in Ω that vanish on $\partial\Omega$
$L^2(\Omega)$	($\equiv H^0$) space of square-integrable functions in Ω
$L^1(\Omega)$	space of integrable functions in Ω
H_γ	Hilbert space defined by the Gaussian measure γ (Cameron-Martin space)
$\ u\ _{L^2(\Omega)}$	L^2 -norm of u in Ω
$\ u\ _{H^k(\Omega)}$	($\equiv \sum_{i=0}^k \ \nabla^i u\ _{L^2(\Omega)}$) H^k -norm of u in Ω
$ u _{H^1(\Omega)}$	($\equiv \ \nabla u\ _{L^2(\Omega)}$) H^1 -seminorm of u in Ω
$\langle \cdot, \cdot \rangle$	inner-product in L^2

Acronyms / Abbreviations

MRI	Magnetic Resonance Imaging
MRV	Magnetic Resonance Velocimetry
MRA	Magnetic Resonance Angiography
CT	Computed Tomography
PIV	Particle Image Velocimetry

Chapter 1

Introduction

Starting from the physiology of the circulatory system we briefly discuss the physical modeling of haemodynamics in large blood vessels. Next, we describe the experimental technique of magnetic resonance velocimetry, the basic principles of signal acquisition and reconstruction, and its applications in fluid dynamics. Lastly, we present a prototype inverse problem in haemodynamics, and review the relevant literature.

1.1 Fluid mechanics of large blood vessels

The mammalian arterial tree consists of a complicated network of blood vessels within which flow conditions and characteristic length scales vary greatly. The main and largest blood vessel of the cardiovascular system is the *aorta*. The initial part of the human aorta is connected to the left ventricle of the heart. It ascends for ~ 3 cm before starting a complicated three-dimensional turn of about 180 degrees (aortic arch), giving out three branches that supply blood to the head and the arms. Then, it follows a relatively straight path descending to the abdomen where it branches out again to support the major organs, and terminates in the lower abdomen, where the iliac arteries start.

The wall of large arteries is composed of three main layers, namely *tunica intima*, *media* and *externa*, with 50% of the material being elastin, smooth muscle fibres and collagen, and the rest being water. The combined wall structure can be modeled as a thin-walled cylinder of incompressible, viscoelastic orthotropic material¹. However, even if the elastic properties of some of the essential materials are known, there are considerable uncertainties regarding the activity of the muscle fibre (contracted or relaxed), and the mechanical properties of the tunica externa, which is tethered to the surrounding tissue [64].

Blood is a suspension of cells in plasma. On average, 45% of blood's volume consists of red blood cells (hematocrit), 1% of white cells and platelets, and the rest is plasma. Even if the contribution of the platelets to the mechanical properties of blood appears negligible at first sight, they take an active role in blood clotting and can thus become important [32]. The red cells are biconcave elastic disks², with a diameter of approximately 6 to 8 μm and are more

¹Classical laminate theory may be used to compute the equivalent mechanical properties.

²Interestingly, their shape minimizes the total bending energy (Willmore energy).

numerous than any other blood cell. Consequently, it is these cells that together with plasma dictate blood's mechanical properties. Although plasma alone behaves as a homogeneous Newtonian fluid, blood as a whole can be considered homogeneous only for arteries whose diameter exceeds $\sim 100\mu\text{m}$ ³. Also, viscosity is found to be independent of the shear rate ∇u , when $\nabla u > 100\text{ s}^{-1}$ [85]. Since the average shear rate exceeds this value for large arteries we shall assume that blood behaves as an homogeneous Newtonian fluid [64]. Still, this assumption may not be always valid as ∇u oscillates due to the pulsatile character of the flow. The same thinking applies near regions of recirculatory flow, where shear rates may not exceed the aforementioned critical value.

One of the first substantial contributions to the mathematical modeling of blood flow is due to Womersley [86], who derived analytical expressions for the velocity profile in the case of axisymmetric and laminar pulsatile pipe flow, under a given pressure pulse. This effectively extended the theory of Poiseuille flow to unsteady, albeit periodic, flows. Then, Womersley proceeded to treat the problem of pulse wave propagation through thin-walled elastic tubes [87]. This model was further extended by Atabek [2] and Pedley [64], to viscoelastic, orthotropic tubes, tethered to an external rigid structure. By working out the dispersion relation of these fluid-structure interaction problems, one deduces precious information regarding the pulse wave speed and its attenuation, as well as the mass flow rate and the wall shear stresses. Unfortunately, arteries seldom resemble a straight and uniform pipe. On the contrary, arteries are tapered, curved⁴, have varying arterial wall properties and divide into branches (bifurcations). In addition, pulse wave reflection (due to branching) is often important and has to be taken into account. Therefore, to model blood flow in vessels, or parts of the arterial tree, the above theories are generalized and numerically solved [3, 8, 64, 79]. One-dimensional pulse wave transmission models, resulting from lumping properties of the two-dimensional velocity profiles, are reviewed in [79].

Even though the flow is laminar in most parts of the circulatory system, turbulence has been observed in the aorta [59], and in abnormal conditions produced by aneurysms [29, 37] or a stenosis [38, 90]. Due to the complexity of the latter problems, a numerical solution of the three-dimensional Navier–Stokes equations is needed, and the studies usually focus on flow details such as the precise wall-shear stress distribution and the pressure spectra⁵, for an isolated segment of a blood vessel. However, even for these detailed studies, the problem is greatly simplified as there are many physiological conditions that are unknown or difficult to measure.

As patient-specific cardiovascular modeling is gaining ground [77, 58], new approaches to tackle the above problems rely partly on physical models and partly on experimental measurements. Consequently, the focus is not on the theoretical model itself, but on the solution of an *inverse problem* that combines the model and the experiment to infer uncertain physiolog-

³For comparison, the diameter of the descending aorta is about 2 to 3 cm.

⁴An extreme example of a curved artery is the aortic arch.

⁵To indentify and understand heart murmurs (detected with a stethoscope) emanating from an aortic stenosis.

ical model parameters. The inferred parameters are subsequently used to revise the model⁶, rendering it patient-specific, and assist doctors in diagnosing a cardiovascular disease.

1.2 Principles of magnetic resonance imaging/velocimetry

Magnetic resonance imaging (MRI) is a completely non-invasive medical imaging technique that relies on nuclear magnetic resonance. It was Rabi, Bloch and Purcell who observed that atomic nuclei with nonzero nuclear spin (e.g. ^1H , ^{13}C) can absorb radio-frequency pulses, in the presence of a background constant magnetic field \mathbf{B}_0 . Resonance then occurs at (Larmor) frequency $\omega_0 = \gamma B_0$, with γ the gyromagnetic ratio of the resonating nucleus. Nuclear magnetization is described by the Bloch equations, and depends on γ as well as the nuclear spin relaxation times T_1, T_2 , and the external magnetic field experienced by the nuclei. In particular, T_1 and T_2 refers to the longitudinal and transversal relaxation times, respectively, which characterize the return of the nuclear spin system to thermal equilibrium. To acquire an image, we first correlate position with frequency by introducing, in addition to \mathbf{B}_0 , a magnetic field gradient \mathbf{G} . Then, the frequency of resonance is $\omega_0(\mathbf{r}) = \gamma(\mathbf{B}_0 + \mathbf{G} \cdot \mathbf{r})$, with \mathbf{r} being the position vector in \mathbb{R}^3 . Subsequently, we use coils to emit rf-pulse sequences and then measure the nuclear magnetization. The acquired signal S is the Fourier dual of the nuclear spin density ρ since [18]

$$S(\mathbf{k}) = \int_{\mathbb{R}^3} \rho(\mathbf{r}) e^{i\mathbf{k} \cdot \mathbf{r}} d\mathbf{r} \quad , \quad \rho(\mathbf{r}) = \int_{\mathbb{R}^3} S(\mathbf{k}) e^{-i\mathbf{k} \cdot \mathbf{r}} d\mathbf{k} \quad , \quad \mathbf{k} = \gamma \mathbf{G} t \quad .$$

Therefore, the nuclear spin density $\rho(\mathbf{r})$ (medical image) is recovered by an inverse Fourier transformation of the signal $S(\mathbf{k})$, which was sampled in the \mathbf{k} -space. This is the underlying principle of MRI. To measure velocity fields, two separate acquisitions are needed: the first using \mathbf{G} and the second using $-\mathbf{G}$. The accrued phase change of the signal is then directly proportional to the displacement, from which velocity is recovered [19]. This technique is called phase-contrast MRI and is widely used in magnetic resonance velocimetry (MRV) and magnetic resonance angiography (MRA).

There are numerous applications of MRV at different flow conditions, spanning a wide range of disciplines [33, 36]. For example, MRV has been used to measure high Reynolds number turbulent gas flows around airfoils [60] as well as Stokes flow of cytoplasm in plant cells [78]. Rheological properties of non-Newtonian fluids are studied in [31, 9]. In haemodynamics, an early attempt to measure blood flow using MRI can be traced back to 1959 [73]. Since then, MRV techniques have greatly evolved and are now able to provide volumetric velocity data of unsteady blood flows in almost any part of the human body [53]. Still, acquisition (scanning) times are relatively long, ranging from minutes to hours, and scale with resolution, i.e. the sampling density in \mathbf{k} -space.

To reduce scanning times, sparse sampling techniques are used and the full signal is subsequently reconstructed. For instance, Candès *et al.* [20] showed that the true signal $u \in \mathbb{C}^n$ can be reconstructed with very high probability from a (relatively small) set of randomly selected

⁶This process is also known as ‘*data assimilation*’.

frequencies $\{\omega_i\}_{i=1}^k$ when u is a sparse superposition of spikes, i.e. $u(t) = \sum_{\tau \in T} u(\tau)\delta(t - \tau)$ for $T := \{\tau_i\}_{i=1}^\ell$, and $\ell \leq c \frac{k}{\log n}$ for constant $c > 0$. The exact reconstruction u_r is then recovered by solving the optimization problem

$$\min_{u_r} \sum_{t=1}^n |u_r(t)|, \text{ subject to } \hat{u}_r(\omega_i) = \hat{u}(\omega_i) \text{ for } i = 1, \dots, k$$

where $\hat{u} := \mathcal{F}u$, with \mathcal{F} denoting the Fourier transform. Similar results are outlined in [28], and the relevant techniques are known as *compressed sensing*. The application of the above theories was immediate in the field of MRI [52], leading to strategies for k -space (under)sampling and signal reconstruction. Variational approaches for the reconstruction of subsampled signals are reviewed in [7]. The reconstruction problem under study [7] reads

$$\text{find } u_\alpha \text{ that belongs to } \arg \min_u \left(\|\hat{u}^* - \mathcal{S}\mathcal{F}u\|_{\ell^2}^2 + \alpha \mathcal{R}(u) \right),$$

where $\hat{u}^* \in \mathbb{C}^m$ is the undersampled signal ($m < n$), and \mathcal{S} is the sampling pattern operator. Therefore, $\mathcal{S}\mathcal{F}u \in \mathbb{C}^m$ is the element obtained after projecting u on the k -space, and then restricting it on the sampling pattern so that it can be compared with \hat{u}^* . Regarding the Tikhonov regularization term (second term), α is a tuning constant and \mathcal{R} is an appropriate norm of u (or its derivatives) which greatly affects the reconstruction. More precisely, it is \mathcal{R} that encapsulates the prior knowledge, for example how smooth or rough we expect the real signal u to be. In [7], a comparison is made for three different choices of \mathcal{R} , namely, i) total variation⁷, ii) wavelet space coefficient norm, and iii) total generalized variation.

The aforementioned reconstruction process relies only on image processing algorithms, which are quite general and somehow subjective (due to α, \mathcal{R}). However, for magnetic resonance velocimetry some subjectivity can be removed from the reconstruction process by invoking the Navier–Stokes equations⁸. Although MRV data have been assimilated in Navier–Stokes problems recently [47, 34], the data that were used were already reconstructed from the k -space samples. To the best of the author’s knowledge, the problem of reconstructing an MRV signal directly from k -space, with the aid of the Navier–Stokes equations, has not yet been addressed. We discuss an approach to this problem in section 3. Lastly, we stress that reducing scanning times and increasing resolution in MRV brings considerable impact in medical diagnosis⁹ as well as in experimental fluid dynamics and turbulence.

1.3 Inverse problems in cardiovascular fluid mechanics

Inverse problems entwine a physical model with a measurement technique to extract a hidden variable, i.e. one that cannot be directly measured. In haemodynamics, the physical model, hereafter also referred as ‘theoretical twin’, is a Navier–Stokes problem, and the measurement

⁷The total variation (non-smooth) norm is very common in image processing to preserve edges [67].

⁸We can think of this as the ‘theoretical twin’ of the MRV experiment.

⁹Current scanning times of ~ 5 -20 minutes imply the averaging of potentially non-periodic phenomena [53].

technique usually relies on magnetic resonance velocimetry. These problems are particularly important for patient-specific modeling and prognosis. On the one hand, pure physical models of blood flow include several uncertain physiological model parameters (see section 1.1). On the other hand, MRV scans provide only velocity fields, and, depending on the acquisition protocol, a reconstruction of the signal is needed (see section 1.2). Consequently, combining the a priori knowledge with the experiment, yields the possibility of both inferring unknown quantities (e.g. wall-shear stress) and reconstructing (denoising) the MRV signal. The unknown physiological parameters can be grouped in five main categories

- i. **Blood vessel geometry**; $(\Omega, \Gamma, \Gamma_i, \Gamma_o)$.
- ii. **Boundary conditions**; velocity/pressure at inlets (e.g. left ventricle) and outlets $(\mathbf{g}_i, \mathbf{g}_o)$.
- iii. **Pressure pulse-wave**; pressure wave form (f) resulting after reflection, attenuation etc.
- iv. **Fluid model**; kinematic viscosity ν , stress tensor relations $\boldsymbol{\tau} = f(\nu, \nabla \mathbf{u})$ etc.
- v. **Elastodynamics**; elastic modulus of internal elastic lamina, endothelium, tethering etc.

For large blood vessels, we can assume that blood behaves as a Newtonian fluid. Then, the effective viscosity ν depends on the hematocrit, which varies among people. Subsequently, if we neglect the problem of elastodynamics, the physiological parameters (i.)-(iv.) are all taken into account in the following Navier–Stokes problem ¹⁰

$$\left\{ \begin{array}{ll} \mathbf{u} \cdot \nabla \mathbf{u} - \nu \Delta \mathbf{u} + \nabla p = \mathbf{f} & \text{in } \Omega \\ \nabla \cdot \mathbf{u} = 0 & \text{in } \Omega \\ \mathbf{u} = \mathbf{0} & \text{on } \Gamma \\ (-\nu \nabla \mathbf{u} + pI) \cdot \boldsymbol{\nu} = \mathbf{g}_i & \text{on } \Gamma_i \\ (-\nu \nabla \mathbf{u} + pI) \cdot \boldsymbol{\nu} = \mathbf{g}_o & \text{on } \Gamma_o \end{array} \right. . \quad (1.1)$$

Note that, although we neglected the elastodynamics, we have not fixed the blood vessel geometry. Therefore, for unsteady flows, we can still infer the movement of the geometry and its influence on the velocity field, but we cannot infer the elastic properties of the blood vessel. Also, it is possible to modify the boundary conditions on Γ_i, Γ_o , e.g. we could have specified a Dirichlet boundary condition on Γ_i . The boundary value problem (1.1) is what we consider to be a theoretical twin of a magnetic resonance velocimetry experiment.

It has long been known that wall-shear stress $\boldsymbol{\tau}_w$ affects the endothelial cell structure [64], and that abnormal magnitudes or distributions of $\boldsymbol{\tau}_w$ are correlated with the onset, or the progress, of certain cardiovascular diseases (e.g. aneurysms and atherosclerosis) [43, 58]. Therefore, a problem of interest is to infer the $\boldsymbol{\tau}_w$ -distribution from MRV scans. To do so, however, we first need to match the solution \mathbf{u} of (1.1) to the MRV data \mathbf{u}^* . In a recent study [47], the problem of controlling the Dirichlet (velocity) boundary condition on Γ_i , to match \mathbf{u} to \mathbf{u}^* , is treated for steady blood flows. MRV measurements are used only in a restricted

¹⁰This is a steady problem. The same parameters are involved in an unsteady, albeit periodic, problem. For an unsteady (non-periodic) problem, the initial condition on velocity is added to the unknown model parameters.

domain $\Omega_s \Subset \Omega$ which excludes the near-wall regions¹¹. The problem is formulated using optimal control theory for the incompressible Navier–Stokes equations¹². The discrepancy $\mathbf{u} - \mathbf{u}^*$ is measured with the $L^2(\Omega_s)$ -norm and additional regularization terms are used for the control. The goal is to improve near-wall velocity predictions in order to measure τ_w and to assist in the clinical assessment of endothelial disorders. The same formulation is extended to unsteady, albeit periodic, flows in [45, 46]. The authors use the harmonic balance method for the temporal discretization of the Navier–Stokes problem. They express the time evolution of the velocity field as a superposition of sinusoids, and form the linear system of equations using a collocation method. They report that their method is 15 times faster than its traditional unsteady counterpart, and that, for spatiotemporal MRV, the method requires between 17 and 25 time instances, corresponding to at least 8 harmonics. In [34] the problem of inferring both the Dirichlet Γ_i boundary condition and the initial condition $\mathbf{u}(x, t)|_{t=0}$ ¹³ is studied for unsteady blood flows and 4D MRV data. Nitsche’s method [61] is used to enforce the Dirichlet boundary condition in a weak sense, and the adjoint state of the discrete system is tracked by automatic differentiation. Applications relating to cerebral aneurysms for 2D and 3D unsteady flows are demonstrated, and an in-depth robustness study follows regarding the effect of: i) incomplete MRV data, ii) noise and iii) regularization (tuning) constants. We note that the above studies [47, 45, 46, 34] consider rigid boundaries and a Newtonian fluid, and that for the algorithms to work, a geometric representation of the blood vessel is required as an input.

To find the geometry of the blood vessel, computed tomography (CT) or MRA is often used and the acquired signal is subsequently reconstructed, segmented, and smoothed. This process not only requires substantial effort and the design of an additional experiment, but it also introduces geometric uncertainties [58, 68], which, in turn, affect the predictive confidence of arterial τ_w -distributions and their mappings [43]. A more consistent approach to this problem, would be to include the blood vessel geometry in the reconstruction process. In this way, the theoretical twin can better adapt to the MRV experiment and correct the geometric errors. Then, only a starting guess is needed for the blood vessel geometry, which can be taken by automatically segmenting¹⁴ the MRV data to obtain an approximation of the blood vessel boundary. We discuss the theory of this problem in section 2.1, and apply it to simpler models such as the Poisson and the Stokes equation in two-dimensions.

Inverse problems in fluid mechanics, also known as optimal control problems for (1.1), or data assimilation problems, have been intensively studied during the last decade, mainly due to the increase of available computing power. Recent applications in fluid mechanics range from the forcing inference problem [41], to the reconstruction of particle image velocimetry (PIV) signals [35] and the identification of optimal sensor arrangements [57, 83]. Regularization methods for ill-posed problems are reviewed in [75] and [6], from a Bayesian and a variational

¹¹MRV measurements are blurry near the wall imposing difficulties in the definition of a boundary.

¹²They solve (1.1) but with Dirichlet boundary condition on Γ_i , $\mathbf{g}_o = \mathbf{0}$ and $\mathbf{f} = \mathbf{0}$.

¹³The authors note that periodic (in time) boundary conditions should be used, but this type of boundary condition was not available in their software.

¹⁴Image segmentation is the process of partitioning an image into multiple regions.

perspective, respectively, and the well-posedness of such Bayesian inverse problems is addressed in [22].

1.4 Conclusions and Research objectives

1. Reduce signal acquisition time and increase resolution in magnetic resonance velocimetry.

As we discussed in section 1.2, to reconstruct an MRV signal from the \mathbf{k} -space, general image processing algorithms are mainly used. We cannot expect, however, that a general image processing algorithm will respect a conservation law (eg. incompressibility) or the boundary conditions (e.g. no-slip condition, law of the wall etc.). Consequently, we conclude that a priori knowledge should be used in the form of a theoretical twin of the MRV experiment. We assume that a good choice for a theoretical twin is an appropriate Navier–Stokes problem. Consequently, we intend to reconstruct undersampled MRV signals in physical (\mathbf{x}) or frequency (\mathbf{k}) space and study the implications on signal loss, recovery, and acquisition time reduction.

2. Infer unknown physiological parameters that cannot be measured by other means.

By combining MRV measurements with a theoretical twin, we form an inverse problem. The solution to the inverse problem provides valuable information for patient-specific modeling and medical diagnosis. After reviewing recent works in this field [47, 45, 46, 34] we observe that these studies presume that there is an available geometric representation of the blood vessel, obtained through an additional experiment (eg. CT, MRA). We believe that this process not only introduces geometric errors, but it can lead to inconsistencies where the theoretical twin and the MRV experiment are actually defined on slightly different geometries. Even worse, for real blood flow scans in the aorta, there are significant motions experienced by the blood vessels in the vicinity of the heart, or due to breathing movements. Then the definition of a fixed boundary can only be taken by averaging or after compensating for the motion [69]. Consequently, we build upon previous work by treating the blood vessel geometry as an additional unknown parameter. Observe that the two problems are intertwined; that is, the theoretical twin used to reconstruct the signal is also used to infer the uncertain, or ‘hidden’, physiological parameters.

In the following sections we show how to formulate an inverse problem for the reconstruction of the blood vessel geometry when the theoretical twin is based on a Poisson problem. Next, we show that the method naturally extends to the Stokes problem. For practical inverse problems there is often more than one unknown parameter. Therefore, in the last section we study problems with multiple unknowns, and derive the sensitivity of the inverse problem to model parameters such as the kinematic viscosity ν , the forcing term \mathbf{f} and the inlet boundary condition \mathbf{g} . We mainly consider the Stokes problem as the theoretical twin since the extension to the Navier–Stokes problem (1.1) is currently under development.

Chapter 2

Reconstruction of unknown quantities

The very purpose of formulating a solution to an inverse problem is to extract information about a hidden quantity (one that cannot be directly measured) by combining knowledge obtained from a physical experiment, with its associated ‘theoretical twin’. For instance, let \mathbf{u}^* be the measurement of a velocity field inside or around an object Ω^* , and \mathbf{u} the corresponding prediction using a physical model such as the Navier-Stokes equations with appropriate boundary conditions. Then, the process of inferring the viscosity of the fluid ν so that $\mathbf{u}^* \simeq \mathbf{u}(\nu)$, is an inverse problem. In the sections to follow we study problems where the hidden quantities of interest are the geometry of the object Ω^* , the viscosity of the fluid ν , the unknown (additional) body forces \mathbf{f} that are exerted on the fluid, and the boundary conditions \mathbf{g} . We also keep in mind that in haemodynamics Ω^* would correspond to the blood vessel, ν to blood viscosity, \mathbf{f} to the force due to the pressure gradient, and \mathbf{g} to the pressure at the inlet boundary.

2.1 Shape of the object

We derive an algorithm that infers the shape of an object Ω^* , embedded in an image $I \subset \mathbb{R}^2$. The image I depicts the signal u^* , acquired from a magnetic resonance velocimetry scan, and it is reasonable to assume that a physical model describes the fluid motion inside or around Ω^* . Using this physical model we construct a boundary value problem having solution u in $\Omega \simeq \Omega^*$ and we find the object Ω that minimizes a suitable norm for the discrepancy $u - u^*$. We first describe the shape inference algorithm in detail for the Poisson problem, and later on we discuss its extension to the Stokes problem.

2.1.1 Shape inference using the Poisson equation

Assuming Poiseuille flow, the Navier-Stokes equations simplify to a Poisson boundary value problem. However, to leverage this physical model, a domain of solution Ω has to be specified since the true shape of the object is not known beforehand. This leads to an optimal control problem for Ω^* whose formulation follows.

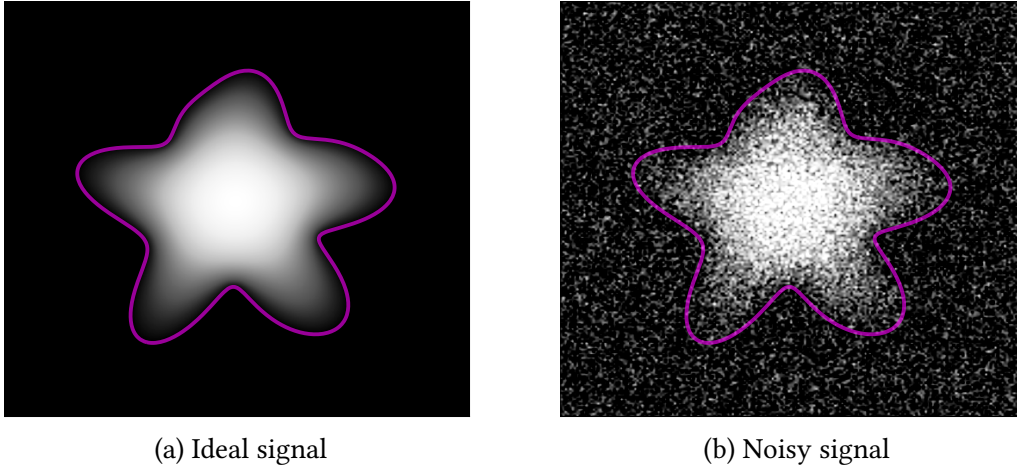


Fig. 2.1 Two images I depicting velocity magnitude u^* (synthetic MRV data). The boundary $\partial\Omega^*$ (purple curve) is a ‘hidden’ quantity, which is to be inferred.

I Shape derivative of the error functional

The discrepancy between u and u^* is measured using the functional

$$\mathcal{J}(u) = \frac{1}{2} \int_I (u - u^*)^2 = \frac{1}{2} \int_{\Omega} (u - u^*)^2 + \frac{1}{2} \int_{I \setminus \Omega} (u - u^*)^2 \quad . \quad (2.1)$$

Its corresponding shape derivative, subject to a speed field \mathcal{V} , is

$$\begin{aligned} D_{\mathcal{V}} \mathcal{J}(u)(\mathcal{V}) &= \frac{1}{2} \left(\int_{\Omega} ((u - u^*)^2)' + \int_{\partial\Omega^+} (u - u^*)^2 \mathcal{V} \cdot \nu + \int_{I \setminus \Omega} (u^*)^2' + \int_{\partial\Omega^-} (u - u^*)^2 \mathcal{V} \cdot \nu \right) \\ &= \int_{\Omega} (u - u^*) u' + \frac{1}{2} \int_{\partial\Omega^+} (u - u^*)^2 \mathcal{V} \cdot \nu - \frac{1}{2} \int_{\partial\Omega^+} (u - u^*)^2 \mathcal{V} \cdot \nu \\ &= \int_{\Omega} (u - u^*) u' \end{aligned} \quad (2.2)$$

where u' is the shape derivative of u with respect to a \mathcal{V} -perturbation of Ω .

II The field of shape derivatives

Starting with the Poisson problem

$$\begin{cases} -\Delta u = f & \text{in } \Omega \\ u = 0 & \text{on } \partial\Omega \end{cases} \quad (2.3)$$

for $f \in C^2(\Omega)$, the weak form for $f \in L^2(\Omega)$ is

$$\int_{\Omega} \nabla u \nabla \phi = \int_{\Omega} f \phi \quad , \quad \phi \in H_0^1(\Omega) \quad . \quad (2.4)$$

Considering Ω as a moving domain Ω_τ , $\tau \in [0, \epsilon]$, the shape derivative of (2.4) is

$$\begin{aligned} D_{\mathcal{V}} \left(\int_{\Omega} \nabla u \nabla \phi \right) &= D_{\mathcal{V}} \left(\int_{\Omega} f \phi \right) \\ \int_{\Omega} (\nabla u \nabla \phi)' + \int_{\partial\Omega} (\nabla u \nabla \phi)(\mathcal{V} \cdot \nu) &= \int_{\Omega} (f \phi)' + \int_{\partial\Omega} (f \phi)(\mathcal{V} \cdot \nu) \\ \int_{\Omega} \nabla u' \nabla \phi &= \int_{\Omega} f' \phi \quad , \end{aligned} \quad (2.5)$$

while a perturbation of the Dirichlet boundary condition gives

$$\begin{aligned} D_{\mathcal{V}} \left(\int_{\partial\Omega} u \phi \right) &= \int_{\partial\Omega} (u \phi)' + (\nu \cdot \nabla + \kappa) u \phi (\mathcal{V} \cdot \nu) \\ &= \int_{\partial\Omega} u' \phi + (\nu \cdot \nabla (u \phi) + \kappa u \phi) (\mathcal{V} \cdot \nu) \\ &= \int_{\partial\Omega} (u' + (\nu \cdot \nabla u) (\mathcal{V} \cdot \nu)) \phi = 0 \quad , \quad (\text{since } u|_{\partial\Omega} = 0). \end{aligned} \quad (2.6)$$

The above weak forms translate to the following classical boundary value problem for the shape derivatives

$$\begin{cases} -\Delta u' = f' & \text{in } \Omega \\ u' = -(\nu \cdot \nabla u) (\mathcal{V} \cdot \nu) & \text{on } \partial\Omega \end{cases} . \quad (2.7)$$

If the forcing term f does not depend on perturbations of Ω , then $f' \equiv 0$ and (2.7) is a Dirichlet problem for the Laplace equation. Otherwise, if for example f is a pressure gradient that changes when Ω deforms, additional physical knowledge is required to specify the form of f' .

At this point, observe that one can choose a speed field \mathcal{V} to solve the shape derivatives problem (2.7) for u' . Proceeding to compute problem (2.7) for infinitely¹ many speed fields of the form $\mathcal{V} = \delta(x)\nu(x)$, for $x \in \partial\Omega$, where δ denotes the Dirac measure, leads to a brute-force estimation of the shape gradient \mathcal{V}^* of (2.2). Fortunately, there is a much quicker way to find \mathcal{V}^* by solving the adjoint problem.

III Constructing the adjoint problem

Taking the problem (2.7) for u' and integrating by parts twice, we find

$$- \int_{\Omega} u' \Delta v + \int_{\partial\Omega} u' \nabla v \cdot \nu = \int_{\Omega} f' v \quad (2.8)$$

for $v \in H^2(\Omega) \cap H_0^1(\Omega)$. But $u'|_{\partial\Omega}$ is known from the boundary condition of (2.7), thus

$$- \int_{\Omega} u' \Delta v = \int_{\Omega} f' v + \int_{\partial\Omega} (\nu \cdot \nabla u) (\mathcal{V} \cdot \nu) (\nabla v \cdot \nu) \quad . \quad (2.9)$$

¹For a numerical problem the word 'infinite' corresponds to the number of mesh points that discretize $\partial\Omega$.

Subsequently, if we choose v that solves the adjoint problem

$$\begin{cases} -\Delta v = u - u^* & \text{in } \Omega \\ v = 0 & \text{on } \partial\Omega \end{cases} \quad (2.10)$$

the error functional shape derivative (2.2) recasts to the form

$$\int_{\Omega} (u - u^*) u' = - \int_{\Omega} u' \Delta v = \int_{\Omega} f' v + \int_{\partial\Omega} (\nu \cdot \nabla u) (\mathcal{V} \cdot \nu) (\nabla v \cdot \nu) \quad (2.11)$$

for any function u' . In the end,

$$D_{\mathcal{V}} \mathcal{J}(u, v, \tilde{f})(\mathcal{V}) = \langle \tilde{f} + \partial_{\nu} u \partial_{\nu} v, \mathcal{V} \cdot \nu \rangle_{\partial\Omega} \quad (2.12)$$

where

$$\int_{\Omega} f' v = \int_{\partial\Omega} \tilde{f} (\mathcal{V} \cdot \nu)$$

with the existence of \tilde{f} implied by the Hadamard-Zolesio structure theorem for the shape derivative [74, 26, 84]. Hereafter, we take $f' \equiv 0$ and no physical process is identified with f . Restricting our interest in \mathcal{V} 's that can be defined through $\partial\Omega$'s normal vector ν and a scalar function ζ defined on $\partial\Omega$ (Hadamard parameterization), we write $\mathcal{V} = \zeta \nu$ and rewrite (2.12) in its final form

$$\boxed{\langle D_{\mathcal{V}} \mathcal{J}, \zeta \rangle_{\partial\Omega} = \langle \partial_{\nu} u \partial_{\nu} v, \zeta \rangle_{\partial\Omega}}. \quad (2.13)$$

IV Propagating the boundary of Ω

Formula (2.13) provides the functional derivative that drives the geometric gradient flow minimizing $\|u - u^*\|_{L^2(I)}$. In theory, one can simply write

$$x \mapsto x + \tau \zeta^*(x) \nu(x) \quad \text{for every } x \in \partial\Omega \quad (2.14)$$

to explain the deformation of $\partial\Omega$ at given pseudotime $\tau > 0$ and for $\zeta^* = -\partial_{\nu} u \partial_{\nu} v$. However, (2.14), as is, leads to inefficient numerical algorithms because the phrase ‘for every $x \in \partial\Omega$ ’, although very conveniently written, overshadows the difficulty of locating a surface in space.

Here, to tackle this problem, we use signed distance functions ϕ_{\pm} to represent general surfaces (closed curves) in \mathbb{R}^2 . Then the object Ω and its boundary $\partial\Omega$ are identified with a particular function ϕ_{\pm} so that the following holds

$$\Omega = \{x \in \Omega : \phi_{\pm}(x) < 0\} \quad , \quad \partial\Omega = \{x \in \Omega : \phi_{\pm}(x) = 0\} \quad (2.15)$$

Obviously, $\phi_{\pm}(x) > 0$ for points in space that belong neither to Ω nor to its boundary. The above definition does not actually require ϕ_{\pm} to be a distance function but only a signed function, although it is convenient for ϕ_{\pm} to be at least continuous near $\partial\Omega$. Despite this, and the fact that

the distance from $\partial\Omega$ is not involved in any part of the shape inference algorithm, we continue working with signed distance functions (instead of just signed functions).

Consequently, we approximate (2.14) by transporting ϕ_{\pm} under the speed field $\mathcal{V}^* = \zeta^*\nu$. The advection-diffusion initial value problem for $\phi_{\pm}(x, t)$ reads

$$\begin{cases} \partial_t \phi_{\pm} + \nabla \cdot (\phi_{\pm} \mathring{\mathcal{V}}) - \epsilon \Delta \phi_{\pm} = 0 & \text{in } I \times (0, \tau] \\ \phi_{\pm} = (\phi_{\pm})_0 & \text{in } I \times \{t = 0\} \end{cases} \quad (2.16)$$

where $(\phi_{\pm})_0$ denotes the signed distance function of the current domain Ω , $0 < \epsilon \ll 1$ the diffusion coefficient², and $\mathring{\mathcal{V}} := \mathring{\mathcal{V}}^* : I \rightarrow \mathbb{R} \times \mathbb{R}$ is an extension of $\mathcal{V}^* : \partial\Omega \rightarrow \mathbb{R} \times \mathbb{R}$. If we solve (2.16) for $\phi_{\pm}(x, \tau)$ we obtain the implicit representation of the perturbed domain Ω_{τ} , but to do so we first need to extend \mathcal{V}^* to the whole space of the image I . First, observe that $\mathcal{V}^* = \zeta^*\nu$, where both $\zeta^*(x)$ and $\nu(x)$ are defined only on $\partial\Omega$ ³. Therefore, to extend \mathcal{V}^* to I we first try to extend the normal vector ν and then the scalar function ζ^* .

Initially, the normal vector is only known on the surface $\partial\Omega$, but due to the implicit characterization of $\partial\Omega$ through ϕ_{\pm} we can write

$$\mathring{\nu}(x) = \frac{\nabla \phi_{\pm}}{|\nabla \phi_{\pm}|} = \nabla \phi_{\pm} \quad , \quad x \in I \quad (2.17)$$

since ϕ_{\pm} is a distance function, i.e. $|\nabla \phi_{\pm}| = 1$. Then, to compute an extension of the normal vector in I it suffices to compute the gradient of the signed distance function.

In turn, we compute the signed distance function ϕ_{\pm} . The traditional method is to solve a nonlinear hyperbolic equation (wave propagation), namely, the Eikonal equation

$$|\nabla \phi_{\pm}(x)| = 1 \quad \text{subject to} \quad \phi_{\pm}|_{\partial\Omega} = 0 \quad , \quad x \in I. \quad (2.18)$$

Level-set methods are well-studied and described in [63, 13–15, 89]. A numerical algorithm to solve (2.18), the *fast marching method*, is given in [71], having $n \log n$ complexity with n the total number of mesh points. The same algorithm is used to tackle the problem of both extending \mathcal{V}^* and propagating ϕ_{\pm} in [72]. In spite of the above, we choose a different approach, one that relies on the heat equation [23]. The fundamental solution of the heat equation, the heat kernel

$$\Phi(x, t) = (4\pi t)^{-1} e^{-\frac{\|x\|^2}{4t}} \quad , \quad x \in \mathbb{R}^2, t > 0 \quad (2.19)$$

²Adding diffusion to regularize the conservation law $\partial_t u + \nabla \cdot F(u) = 0$ is known as the method of *vanishing viscosity*. This ‘viscosity solution’ as it is called, satisfies a certain entropy condition at the limit $\epsilon \rightarrow 0$ [30].

³Actually, an extension of ζ in Ω is immediately given by (2.13), since both u, v are functions in Ω . But this solves only half the problem, since an extension in I is still needed.

solves $\partial_t \Phi - \Delta \Phi = 0$ for $\lim_{t \rightarrow 0} \Phi = \delta_x$. Varadhan [82] showed that the heat kernel is intimately related to distance by proving that

$$\lim_{t \rightarrow 0} (-2t \log \Phi(x - y, t)) = \|x - y\|^2 \quad , \quad (2.20)$$

and extended his results to Riemannian metrics by considering general diffusion tensors. The same author also proved relation (2.20), and its generalizations, from the viewpoint of stochastic diffusion processes in [81]. The main theorem that we draw from Varadhan's work [82] to justify the use of the heat equation for the approximation of ϕ_{\pm} , slightly readapted and restricted to Euclidean distance, states that

$$d(x, \partial\Omega) = \lim_{\tau_1 \rightarrow 0} \left(-\frac{\sqrt{\tau_1}}{2} \log u(x, \tau_1) \right) \quad , \quad x \in I \quad (2.21)$$

where $d(x, \partial\Omega)$ is the Euclidean distance between any point $x \in I$ and $\partial\Omega$, and u is the solution of heat propagation away from $\partial\Omega$

$$\begin{cases} (I - \tau_1 \Delta)u = 0 & \text{in } I \\ u = 1 & \text{on } \partial\Omega \end{cases} \quad . \quad (2.22)$$

Crane [23] used Varadhan's results to implement a distance function computation algorithm which he called the '*heat method*'. Here, we readapt this algorithm to compute *signed* distance functions ϕ_{\pm} . Therefore, to compute ϕ_{\pm} we first solve (2.22)⁴ for $\tau_1 \ll 1$ ⁵. Finally, ϕ_{\pm} is given by

$$\begin{cases} \Delta \phi_{\pm} = \nabla \cdot X & \text{in } I \\ \partial_{\nu} \phi_{\pm} = X \cdot \nu & \text{on } \partial I \\ \phi_{\pm} = 0 & \text{on } \partial\Omega \end{cases} \quad , \quad \text{where } X = -\text{sgn}(\psi) \frac{\nabla u}{|\nabla u|} \quad (2.23)$$

with X the normalized heat flux and ψ a signed function so that $\psi(x)$ is negative for points x in Ω and positive for x that lie outside of $\bar{\Omega}$. This intermediate step (solution of two Poisson problems (2.22)-(2.23) instead of only one) is taken to ensure that $|\nabla \phi_{\pm}| = 1$. A signed function ψ , if not available, can easily be found by solving $\Delta \psi = 1$ in I subject to $\psi = 0$ on $\partial\Omega$, although this is only needed (seldom if ever) at the very beginning, to bootstrap the shape inference algorithm.

Accordingly, ϕ_{\pm} leads to a natural extension of $\partial\Omega$'s normal vector ν to I through

$$\hat{\nu}(x) = \text{sgn}(\psi)X(x) \quad , \quad x \in I \quad (2.24)$$

⁴Because $\partial\Omega$ is embedded in I , additional boundary conditions must be specified on ∂I to solve (2.22). Choosing zero-Dirichlet or zero-Neumann boundary conditions makes no difference for the asymptotic behaviour of u as $\tau_1 \rightarrow 0$ (see [62], Theorem 1.1). But since $\tau_1 = 10h^2$, for coarse meshes, boundary effects are noticeable. Thus, for coarse meshes we take $u = \frac{1}{2}(u_D + u_N)$ where u_D, u_N are the solutions of (2.22) with zero-Dirichlet and zero-Neumann boundary conditions on ∂I , respectively [23].

⁵For the numerical problem we take $\tau_1 = 10h^2$ with h the mesh size [23].

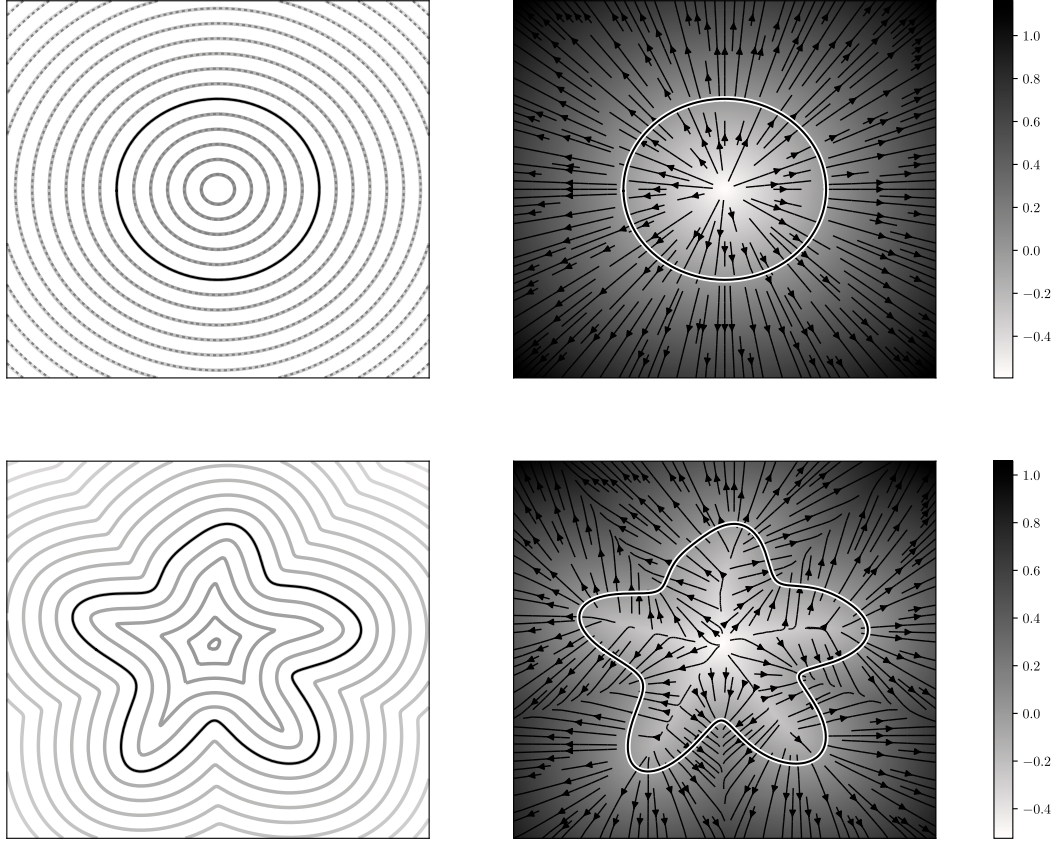


Fig. 2.2 Level-sets of signed distance function ϕ_{\pm} (left) and corresponding normalized heat fluxes X (right) for a circle (upper) and a ‘starfish’ (lower). The boundary $\partial\Omega$ is depicted with a solid black line and the dashed lines in the upper left figure represent the analytical solution.

where the term $\text{sgn}(\psi)$ is used to correct the orientation of $\mathring{\nu}$ so that it points away from $\partial\Omega$. Next, we use the extension $\mathring{\nu}$ to extend ζ^* to $\mathring{\zeta} := \mathring{\zeta}^*$, with the help of the advection-diffusion problem

$$\begin{cases} \partial_t \mathring{\zeta} + \nabla \cdot (\mathring{\zeta} \mathring{\nu}) - \epsilon \Delta \mathring{\zeta} = 0 & \text{in } I \times (0, \tau_{\zeta}] \\ \mathring{\zeta} = \zeta^* & \text{on } \partial\Omega \times (0, \tau_{\zeta}] \\ \mathring{\zeta} \equiv 0 & \text{in } I \times \{t = 0\} \end{cases} \quad (2.25)$$

That is, we convect ζ along the predefined $\mathring{\nu}$ -streamlines and add isotropic diffusion for stabilization (note that $\mathring{\nu}$ -streamlines may have complicated behaviour as in figure 2.2). The timestep τ_{ζ} may be taken large enough to reach a steady-state.

Finally, we recast the initial value problems (2.16) and (2.25) to their corresponding boundary value problem. This is possible due to the linearity of the problem and the fact that the time-dependent solution is of no interest to us. Therefore, instead of problem (2.16) we solve the elliptic problem

$$(I - \tau A_{\mathcal{V}})\phi_{\pm} = (\phi_{\pm})_0 \quad \text{in } I \quad (2.26)$$

where $A_{\mathcal{V}}u := -\epsilon\Delta u + \nabla \cdot (u\overset{\circ}{\mathcal{V}})$. Note that (2.26) propagates ϕ_{\pm} from pseudotime $t = 0$ to $t = \tau$ under the speed field $\overset{\circ}{\mathcal{V}}$. In the same spirit,

$$\begin{cases} (I - \tau_{\zeta}A_{\nu})\overset{\circ}{\zeta} = 0 & \text{in } I \\ \overset{\circ}{\zeta} = \zeta^* & \text{on } \partial\Omega \end{cases} \quad (2.27)$$

replaces (2.25), with $A_{\nu}u := -\epsilon\Delta u + \nabla \cdot (u\overset{\circ}{\nu})$, and describes the propagation of ζ , away from $\partial\Omega$ and along $\overset{\circ}{\nu}$, from pseudotime $t = 0$ to $t = \tau_{\zeta}$.

To summarize, assuming that we start from a signed distance function ϕ_{\pm} , we propagate the boundary of Ω by executing three tasks:

1. Find the heat flux X away from $\partial\Omega$ by solving (2.22) for $\tau_1 \ll 1$.
2. Convect ζ^* along $\overset{\circ}{\nu} = \text{sgn}(\psi)X$, using (2.27) with timestep τ_{ζ} , to obtain $\overset{\circ}{\mathcal{V}} = \overset{\circ}{\zeta}\overset{\circ}{\nu}$.
3. Convect ϕ_{\pm} along $\overset{\circ}{\mathcal{V}}$, using (2.26) with timestep τ , to obtain the new boundary $\partial\Omega_{\tau}$.

Otherwise, if the starting guess is not a signed distance function, or if reinitialization of ϕ_{\pm} is needed, we additionally solve (2.23) immediately after Step 1. As a final note, the above discussion serves two purposes: i) to describe how signed distance functions can be approximated using the heat equation, and ii) to extend the shape gradient $\mathcal{V}^* \equiv \zeta^*\nu$ to the whole domain I and use it to propagate ϕ_{\pm} . Algorithm 1 provides the instructions in order to extend \mathcal{V}^* to $\overset{\circ}{\mathcal{V}}$.

Algorithm 1: Compute_Optimal_Speed_Field $\overset{\circ}{\mathcal{V}}$.

Input: $u, u^*, \phi_{\pm}, \epsilon, \tau_{\zeta}$

begin

1. $v \leftarrow \text{Adjoint_Problem}(u, u^*, \phi_{\pm})$ (equation (2.10))
2. $\zeta^* \leftarrow \text{Shape_Gradient}(u, v, \phi_{\pm})$ (equation (2.13))
3. $\overset{\circ}{\nu} \leftarrow \text{Normal_Vector_Extension}(\phi_{\pm})$ (equation (2.22))
4. $\overset{\circ}{\zeta} \leftarrow \text{Extend_Function}(\zeta^*, \overset{\circ}{\nu}, \phi_{\pm}, \epsilon, \tau_{\zeta})$ (equation (2.27))

Output: $\overset{\circ}{\mathcal{V}} \equiv \overset{\circ}{\zeta}\overset{\circ}{\nu}$

V The shape inference algorithm

The previously discussed methodologies result in an algorithm, compactly presented as algorithm 2, which uses the Poisson equation to infer the shape of an object Ω^* , embedded in an MRV image I . Poiseuille flow, for example, is characterized by a Poisson equation. Therefore, the algorithm is suitable for real-life problems where I depicts the velocity magnitude u^* at a cross section of a general, non-circular, pipe flow. In this section we also assumed that the forcing term f of the Poisson equation, which in Poiseuille flow corresponds to the product of the pressure gradient with inverse viscosity, was constant ($f' \equiv 0$) and known. Later on, we will recall this assumption to treat more general problems where f is an unknown function.

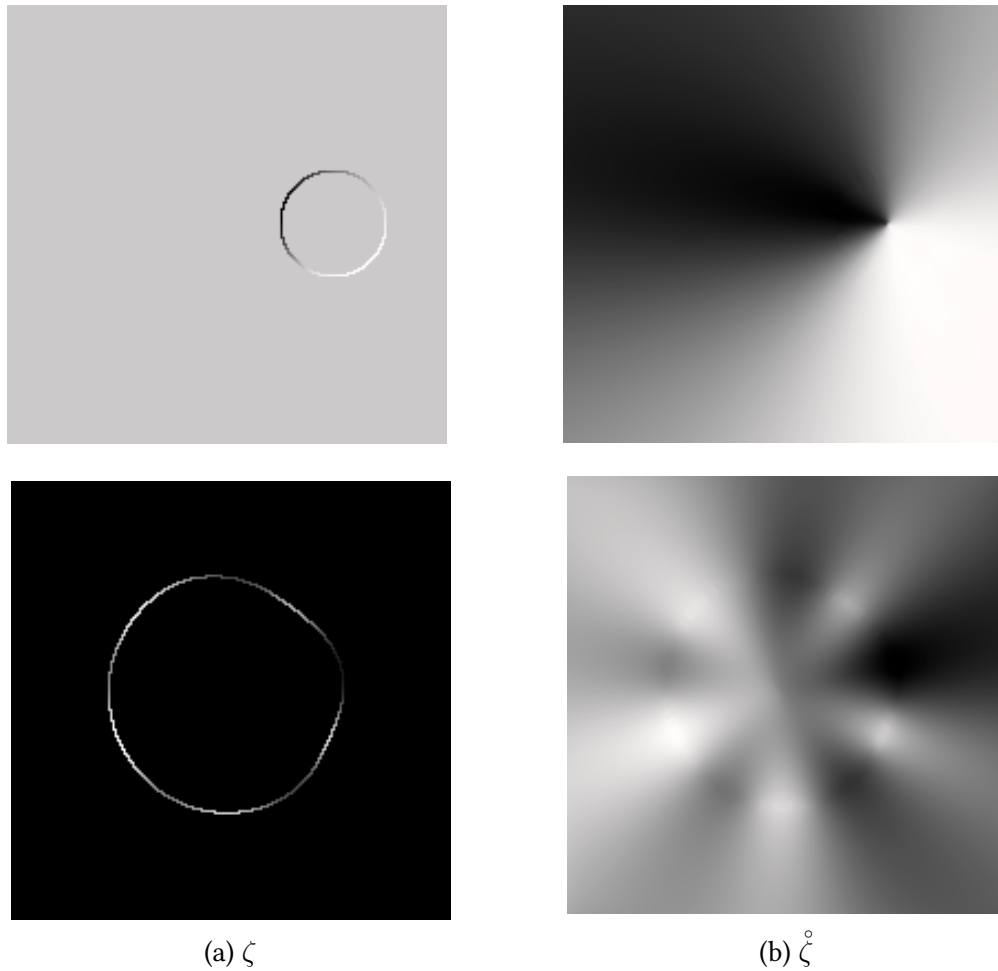


Fig. 2.3 A scalar function $\zeta : \partial\Omega \rightarrow \mathbb{R}$ of the speed field \mathcal{V} , and its extension $\hat{\zeta} : I \rightarrow \mathbb{R}$.

VI Numerics

To solve the previous problems numerically, we adopt an essentially *meshless* method [4], known as the fictitious domain or immersed boundary finite element method. This method presents several advantages over traditional mesh-dependent methods when working with complicated, moving geometries, at the cost of accuracy⁶. In particular, we implement the fictitious domain cut-cell finite element method, introduced by Burman and Hansbo [17, 16] for the Poisson problem, and extended by Massing *et al.* [55] to the Stokes equation. The method uses Nitsche's [61] approach: a consistent and stable way to satisfy Dirichlet boundary conditions on $\partial\Omega$ (the immersed boundary), in a weak sense⁷. However, Burman and Hansbo treated a different problem: the stabilization of the numerical algorithm for arbitrary cut-meshes by introducing a 'ghost-penalty' term. It is often the case that the boundary $\partial\Omega$ cuts the background mesh in such way that cut-cells of very different length scales arise. This leads to ill-conditioned stiffness matrices that prohibit the use of iterative solvers. Fortunately, this problem is rectified with the use of the ghost-penalty term, without sacrificing convergence properties.

⁶In the absence of adaptive meshing algorithms.

⁷Nitsche's results are further generalized in [42].

Algorithm 2: Shape inference for magnetic resonance imaging (Poisson model).**MRV data:** image I depicting u^* , **Model input:** $f, \epsilon, \tau_\zeta, (\phi_\pm)_{i=0}$ **Optimization input:** $\tau_{i=0}$ (initial timestep), ϵ_{tol} (tolerance), i_{max} (maximum iterations), ℓ_{max} (maximum line searches)**begin****Zero-th iteration:** Set $i \leftarrow 0$, solve Poisson problem (2.4) for u_i in Ω_i (defined by $(\phi_\pm)_i$), and evaluate the discrepancy functional (2.1), setting $\mathcal{J}_i \leftarrow \mathcal{J}(u_i)$.**Geometric gradient flow:****while** ($\epsilon \geq \epsilon_{\text{tol}}$ and $i \leq i_{\text{max}}$) **do**1. $\mathcal{V}_i \leftarrow \text{Compute_Optimal_Speed_Field}(u_i, u^*, (\phi_\pm)_i, \epsilon, \tau_\zeta)$ (algorithm 1)**Set** $\ell_{\text{search}} \leftarrow 0$ and **repeat**2. $(\phi_\pm)_{\text{search}} \leftarrow \text{Gradient_Flow}((\phi_\pm)_i, \mathcal{V}_i, \tau_i)$ (equation (2.26))3. $u_{\text{search}} \leftarrow \text{Poisson_Problem}(f, (\phi_\pm)_{\text{search}})$ (equation (2.4))4. $\mathcal{J}_{\text{search}} \leftarrow \mathcal{J}(u_{\text{search}})$ (equation (2.1)) $\tau_i \leftarrow \tau_i/2$ **if** ($\mathcal{J}_{\text{search}} \geq \mathcal{J}_i$) **else** τ_i $\ell_{\text{search}} \leftarrow \ell_{\text{search}} + 1$ **until** ($\mathcal{J}_{\text{search}} < \mathcal{J}_i$ or $\ell_{\text{search}} > \ell_{\text{max}}$) $i \leftarrow i + 1$ **if** ($\ell_{\text{search}} \leq \ell_{\text{max}}$) **then**└ $(\phi_\pm)_i \leftarrow (\phi_\pm)_{\text{search}}, u_i \leftarrow u_{\text{search}}, \mathcal{J}_i \leftarrow \mathcal{J}_{\text{search}}, \tau_i \leftarrow 3\tau_i/2$ **else**└ **terminate** (line search could not find a better solution)└ $\epsilon \leftarrow |\mathcal{J}_i - \mathcal{J}_{i-1}| / \mathcal{J}_i$ **Output:** Reconstructed domain Ω^* minimizing $\|u(\Omega) - u^*\|_{L^2(I)}$, and filtered velocity magnitude $u \simeq u^*$.

Nitsche's method for the Poisson problem $-\Delta u = f$ in Ω , with Dirichlet boundary condition $u|_{\partial\Omega} = g$, takes the form

$$\int_{\Omega} \nabla u \nabla \varphi - \int_{\partial\Omega} \partial_\nu u \varphi + \mathcal{N}(u, \varphi, \gamma) = \int_{\Omega} f \varphi \quad , \quad \varphi \in H^1(\Omega) \quad (2.28)$$

where

$$\mathcal{N}(u, \varphi, \gamma) = \int_{\partial\Omega} -(u - g) \partial_\nu \varphi + \frac{\gamma}{h} (u - g) \varphi \quad (2.29)$$

is Nitsche's term for the weak satisfaction of the Dirichlet boundary condition on $\partial\Omega$, γ is the penalization constant and h the mesh size. We note that Nitsche's term (2.29) is comprised of two terms, the first one enforces symmetry for the bilinear form between u and φ in a consistent way, and the second imposes the penalization to weakly satisfy $u|_{\partial\Omega} = g$. Assume now for simplicity that $u|_{\partial\Omega} = 0$ is the Dirichlet boundary condition. Then we observe that if we take $\varphi \in H_0^1(\Omega)$ (instead of $H^1(\Omega)$) the Poisson problem reduces to its familiar form

$$\int_{\Omega} \nabla u \nabla \varphi = \int_{\Omega} f \varphi \quad , \quad \varphi \in H_0^1(\Omega) \quad . \quad (2.30)$$

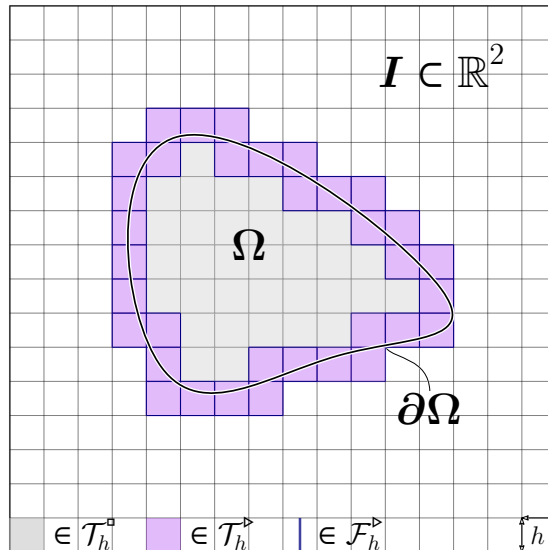


Fig. 2.4 Notation for the fictitious domain method, also known as immersed boundary method.

In the finite element context, $\varphi \in H_0^1(\Omega)$ implies that there exist degrees of freedom (vertices) which rest on the boundary $\partial\Omega$ and that we can force this degrees of freedom (of the test functions) to take the value of the Dirichlet boundary condition. This is not the case in the cut-cell fictitious domain method, where finite elements are arbitrarily cut and the vertices are most likely not to be found lying on the boundary $\partial\Omega$. Therefore, instead of generating new finite elements conforming to $\partial\Omega$ every time that Ω moves, we fix the finite elements (and their degrees of freedom) and use (2.28).

Subsequently, to discretize the problem, we define \mathcal{T}_h to be a tessellation of I produced by square cells (pixels) $K \in \mathcal{T}_h$, having sides of length h . We also define the set of cut-cells \mathcal{T}_h^\dashv consisting of the cells that are cut by the boundary $\partial\Omega$, and \mathcal{T}_h^\square the set of cells that are found inside Ω and which remain intact (not cut) (see figure 2.4). We assume that the boundary $\partial\Omega$ is well-resolved, i.e. $\ell_{\partial\Omega}/h \gg 1$ with $\ell_{\partial\Omega}$ the smallest length scale of $\partial\Omega$. For the detailed assumptions on $\partial\Omega$ we cite [17]. Next, to every cell a bilinear quadrilateral finite element \mathcal{Q}_1 is assigned, and this generates the discretized space

$$V_h = \left\{ u_h \in C^0(I) \text{ such that } u_h|_K \in \mathcal{Q}_1 \text{ for all } K \in \mathcal{T}_h \right\} \quad (2.31)$$

where $\mathcal{Q}_1 = \left\{ \sum_\ell c_\ell p_\ell(x) q_\ell(y) \text{ for polynomials } p_\ell, q_\ell \text{ of degree } \leq 1 \right\}$. Then, the discretized Dirichlet problem for the Poisson equation reduces to finding $u_h \in V_h$ such that

$$a(u_h, \varphi_h) + j(u_h, \varphi_h) = i(\varphi_h) \quad \text{holds for all } \varphi_h \in V_h \quad (2.32)$$

for the bilinear forms a, j and the linear functional i given by

$$a(u_h, \varphi_h) := \int_{\Omega} \nabla u_h \nabla \varphi_h + \int_{\partial\Omega} -\partial_\nu u_h \varphi_h - u_h \partial_\nu \varphi_h + \frac{\gamma}{h} u_h \varphi_h \quad (2.33a)$$

$$i(\varphi_h) := \int_{\Omega} f \varphi_h + \int_{\partial\Omega} -g \partial_\nu \varphi_h + \frac{\gamma}{h} g \varphi_h \quad (2.33b)$$

$$j(u_h, \varphi_h) := \sum_{F \in \mathcal{F}_h^\triangleright} \int_F \gamma_1 h [\nabla u_h][\nabla \varphi_h] \quad (2.33c)$$

For the ghost-penalty (2.33c), γ_1 is a penalization constant and $[\nabla \cdot]$ denotes the jump of the gradient at face F . We further define $\mathcal{F}_h^\triangleright$ to be the set of element faces that are shared by two cells K, K' , where at least one of them belongs to the cut-cell set $\mathcal{T}_h^\triangleright$ (see figure 2.4). The next step is to take a basis $\{\varphi_i\}_{i=1}^n$ of V_h and write $u_h = \sum_{j=1}^n u_j \varphi_j$ and $\varphi_h = \sum_{i=1}^n \varphi_i$ to find that

$$A_{ij} u_j = F_i \quad (2.34)$$

is a finite dimensional approximation of (2.32), where

$$A_{ij} := a(\varphi_j, \varphi_i) + j(\varphi_j, \varphi_i) \quad , \quad F_i := i(\varphi_i) \quad (2.35)$$

for $i, j = 1, \dots, n$. To compute the matrix A_{ij} and the vector F_i , the integrals of (2.33a)-(2.33c) have to be computed. For cells $K \in \mathcal{T}_h^\square$ we employ standard Gaussian quadrature while for cut-cells $K \in \mathcal{T}_h^\triangleright$, where integration must be considered only for the intersection $K \cap \Omega^8$, we use Mirtich's approach [56]. Mirtich's approach relies on the divergence theorem and simply replaces the integral over $K \cap \Omega$ with an integral over $\partial(K \cap \Omega)$. The boundary integral on $\partial(K \cap \Omega)$ is then easily computed using one-dimensional Gaussian quadrature. The adaptation of this method in the context of finite elements is further discussed in [54]. Standard one-dimensional Gaussian quadrature is also used for any boundary (or face) integral appearing in (2.33a)-(2.33c).

Most of the boundary value problems of subsection 2.1.1 reduce to a Poisson problem in Ω with Dirichlet boundary conditions on $\partial\Omega$. For other problems, such as problem (2.26), which defines the propagation of ϕ_\pm in the whole space I (no immersed boundary involved) through a linear advection-diffusion equation, standard finite element methods are used [12] and are not further discussed here.

VII Results

We conclude this subsection by presenting the results of a shape inference problem with synthetic (artificial) MRV data. To generate the MRV data u^* (image I), we solve the Poisson equation in a known starfish-shaped domain Ω^* embedded in $I \equiv [-1.25, 1.25]^2$, and impose zero Dirichlet boundary conditions on $\partial\Omega^*$ (figure 2.5). Thus, Ω^* serves as the ground truth,

⁸Note that an intersection of a square with a line can result in many different geometric shapes.

and is given by the polar coordinates

$$\rho(\theta) = 0.7 - 0.175 \cos(5\theta) - 0.05 \cos(6\theta) + 0.03 \sin(9\theta) \quad , \quad \theta \in [-\pi, \pi) \quad . \quad (2.36)$$

The initial domain Ω_0 is given by an offset disk, characterized by the signed distance function

$$(\phi_{\pm})_0 = -0.3 + \sqrt{(x - 0.6)^2 + y^2}, \quad x, y \in I \quad . \quad (2.37)$$

For this test case we pick Ω_0 to be far enough from Ω^* to test the robustness of the algorithm. However, for real applications, it would be more practical to use a general image segmentation algorithm for the initial guess Ω_0 . The rest of the parameters, needed to execute the algorithm and solve the numerical problems, are summarized in table 2.1. As a final note, the choice of initial timestep $\tau_{i=0}$, which controls the displacement of $\Omega_{i=0}$, will depend on the speed \mathcal{V}° . Here, the initial timestep corresponds to a normalized gradient, i.e. after the second step of algorithm 1, we normalize ζ^* .

Table 2.1 Parameters for the Poisson shape inference algorithm (algorithm 2).

Model input			Optimization input				Numerics		
f	ϵ	τ_ζ	$\tau_{i=0}$	ϵ_{tol}	i_{max}	ℓ_{max}	Resolution (n)	γ	γ_1
1.0	0.005	15.0	0.1	10^{-6}	100	10	200×200 px	10.0	1.0

Figure 2.5 depicts the results of the algorithm for both ideal⁹ MRV data u^* (Poisson solution, subfigure 2.5a) and noisy MRV data (Poisson solution corrupted by Gaussian white noise, subfigure 2.5b). In the case where the signal is ideal, the reconstructed domain Ω_{100} closely resembles the ground truth Ω^* . Although we can discern a discrepancy between Ω_{100} and Ω^* , particularly at the lower left tip of the starfish, this error on the domain geometry induces a very small error for the velocity magnitude $u - u^*$. Consequently, the shape inference algorithm is rather insensitive to this error, since, after all, we have formulated a problem for the minimization of $\|u - u^*\|_{L^2(I)}$ (subfigure 2.5c). The noisy signal presents signal to noise ratios (SNR) ranging from 0, near the boundary $\partial\Omega^*$, to approximately 14 near the center of Ω^* , where the maximum of u is achieved. For this case, to counteract the roughing effect of noise we use a viscosity coefficient of $\epsilon = 0.0125$ (instead of the ‘default’ value written in table 2.1). The reconstructed domain Ω_{56} is depicted in subfigure 2.5b. From subfigure 2.5d we see that the algorithm has done most of its work in about 10 iterations and does not progress further due to noise. The same happens for the ideal signal, where the reconstruction reaches the starfish shape during the first 10 to 20 iterations, and then very small improvements are made around the tips of the starfish. This stiff behaviour is due to the nonlinearity of the geometric flow problem and the poor choice of the optimization algorithm, which is a simple steepest descent with dynamic stepsize¹⁰.

⁹We refer to the noiseless signal as ‘ideal’.

¹⁰A quasi-Newton optimization algorithm (e.g. BFGS) will be considered in future work.

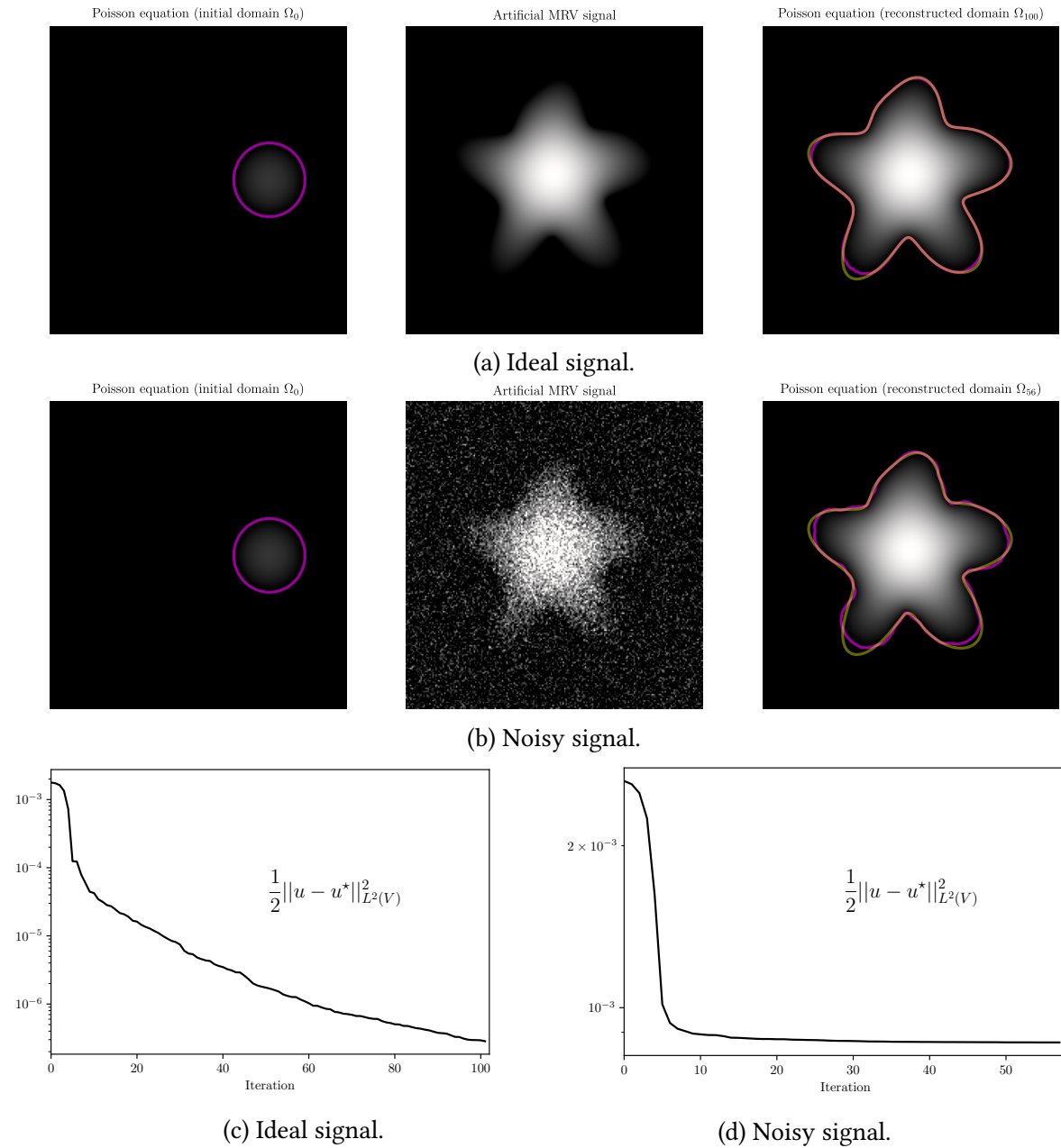


Fig. 2.5 Inferring the shape of an object Ω^* from (synthetic) MRV data, using the Poisson equation. The purple line denotes the shape of the reconstructed domain while the yellow line depicts the ground truth (where the lines overlap they seem orange).

2.1.2 Extension to the Stokes problem

We continue working with the error functional (2.1), but we now write

$$\mathcal{J}(\mathbf{u}) = \frac{1}{2} \|\mathbf{u} - \mathbf{u}^*\|_{L^2(I)}^2 = \frac{1}{2} (\|u_1 - u_1^*\|_{L^2(I)}^2 + \|u_2 - u_2^*\|_{L^2(I)}^2) \quad (2.38)$$

where $\mathbf{u} = (u_1, u_2)$ and $\mathbf{u}^* = (u_1^*, u_2^*)$ are two-dimensional vector fields, and we proceed to derive the problem for the shape derivatives.

I The field of shape derivatives

The Stokes boundary value problem

$$\begin{cases} -\nu\Delta\mathbf{u} + \nabla p = \mathbf{f} & \text{in } \Omega \\ \nabla \cdot \mathbf{u} = 0 & \text{in } \Omega \\ \mathbf{u} = \mathbf{0} & \text{on } \Gamma \\ -\nu\partial_\nu\mathbf{u} + p\boldsymbol{\nu} = \mathbf{g} & \text{on } \Gamma_i \\ -\nu\partial_\nu\mathbf{u} + p\boldsymbol{\nu} = \mathbf{0} & \text{on } \Gamma_o \end{cases} \quad (2.39)$$

describes the motion of a fluid where inertial forces are negligible compared to the viscous forces, with ν the kinematic viscosity¹¹, \mathbf{u} the velocity of the fluid and p the pressure. We consider Neumann, or *natural*, boundary conditions at both the inlet Γ_i and the outlet Γ_o , and no-slip condition at the walls Γ ¹². To find the corresponding shape derivatives problem we start with the weak form of (2.39)

$$\int_{\Omega} \nu \nabla \mathbf{v} : \nabla \mathbf{u} + \int_{\Gamma} \mathbf{v} \cdot (-\nu\partial_\nu\mathbf{u} + p\boldsymbol{\nu}) - \int_{\Omega} (\nabla \cdot \mathbf{v})p - \int_{\Omega} q(\nabla \cdot \mathbf{u}) = \int_{\Omega} \mathbf{v} \cdot \mathbf{f} + \int_{\Gamma_i} \mathbf{v} \cdot \mathbf{g} \quad (2.40)$$

which holds for all test functions $\mathbf{v} \in H^1(\Omega) \times H^1(\Omega)$, with \mathbf{v} also vanishing at Γ , and $q \in L^2(\Omega)$. Using the same methodology as in section 2.1.1, we recover the problem for the shape derivatives (\mathbf{u}', p') of (\mathbf{u}, p) , due to \mathcal{V} -perturbations of Ω .

$$\begin{cases} -\nu\Delta\mathbf{u}' + \nabla p' = \mathbf{f}' & \text{in } \Omega \\ \nabla \cdot \mathbf{u}' = 0 & \text{in } \Omega \\ \mathbf{u}' = -\partial_\nu\mathbf{u}(\mathcal{V} \cdot \boldsymbol{\nu}) & \text{on } \Gamma \\ -\nu\partial_\nu\mathbf{u}' + p'\boldsymbol{\nu} = \mathbf{g}' & \text{on } \Gamma_i \\ -\nu\partial_\nu\mathbf{u}' + p'\boldsymbol{\nu} = \mathbf{0} & \text{on } \Gamma_o \end{cases} \quad (2.41)$$

Using problem (2.41), one can compute the shape derivatives (\mathbf{u}', p') for given perturbation \mathcal{V} . This, however, only provides a trial-and-error approach to finding perturbations \mathcal{V} that reduce the cost functional (2.38)¹³. Instead, we seek the perturbation \mathcal{V}^* that maximizes $D_{\mathcal{V}} \mathcal{J}(\mathbf{u})(\mathcal{V})$, obtained through an adjoint problem.

II Constructing the adjoint problem

Multiplying the shape derivatives problem (2.41) with test (adjoint) functions (\mathbf{v}, q) we obtain

$$\int_{\Omega} \mathbf{v} \cdot (-\nu\Delta\mathbf{u}' + \nabla p' - \mathbf{f}') - \int_{\Omega} q(\nabla \cdot \mathbf{u}') = \mathbf{0} \quad . \quad (2.42)$$

¹¹Hereafter we use ν to denote kinematic viscosity and $\boldsymbol{\nu}$ to denote the unit normal vector of a surface.

¹² $\partial\Omega = \Gamma \cup \Gamma_i \cup \Gamma_o$.

¹³Or a brute-force (also known as finite-difference) approach, described in the previous section.

Integrating by parts and setting $\nabla \cdot \mathbf{v} = 0$ in Ω , and after grouping terms, one finds

$$\int_{\Omega} \nu \nabla \mathbf{v} : \nabla \mathbf{u}' + \int_{\partial\Omega} \mathbf{v} \cdot (-\nu \partial_{\nu} \mathbf{u}' + p' \boldsymbol{\nu}) + \int_{\Omega} \nabla q \cdot \mathbf{u}' - \int_{\partial\Omega} q(\mathbf{u}' \cdot \boldsymbol{\nu}) = \int_{\Omega} \mathbf{v} \cdot \mathbf{f}' . \quad (2.43)$$

After taking into account all three boundary conditions of (2.41), and setting $\mathbf{v} = \mathbf{0}$ on Γ , (2.43) becomes

$$\begin{aligned} \int_{\Omega} \nu \nabla \mathbf{v} : \nabla \mathbf{u}' + \int_{\Omega} \nabla q \cdot \mathbf{u}' - \int_{\partial\Omega \setminus \Gamma} q(\mathbf{u}' \cdot \boldsymbol{\nu}) \\ = - \int_{\Gamma_i} \mathbf{v} \cdot \mathbf{g}' + \int_{\Gamma} -q(\partial_{\nu} \mathbf{u} \cdot \boldsymbol{\nu})(\boldsymbol{\nu} \cdot \boldsymbol{\nu}) + \int_{\Omega} \mathbf{v} \cdot \mathbf{f}' . \end{aligned} \quad (2.44)$$

Subsequently, we integrate by parts and use the Γ -boundary condition of (2.41) one more time to obtain

$$\begin{aligned} \int_{\Omega} (-\nu \Delta \mathbf{v} + \nabla q) \cdot \mathbf{u}' - \int_{\partial\Omega \setminus \Gamma} (-\nu \partial_{\nu} \mathbf{v} + q \boldsymbol{\nu}) \cdot \mathbf{u}' \\ = \int_{\Gamma} (\nu \partial_{\nu} \mathbf{v} \cdot \partial_{\nu} \mathbf{u} - q \partial_{\nu} \mathbf{u} \cdot \boldsymbol{\nu})(\boldsymbol{\nu} \cdot \boldsymbol{\nu}) - \int_{\Gamma_i} \mathbf{v} \cdot \mathbf{g}' + \int_{\Omega} \mathbf{v} \cdot \mathbf{f}' \end{aligned} \quad (2.45)$$

and require that $-\nu \partial_{\nu} \mathbf{v} + q \boldsymbol{\nu} = \mathbf{0}$ on $\Gamma_i \cup \Gamma_o$, so that we can finally write

$$\begin{aligned} \int_{\Omega} (-\nu \Delta \mathbf{v} + \nabla q) \cdot \mathbf{u}' = \int_{\Gamma} (\nu \partial_{\nu} \mathbf{v} \cdot \partial_{\nu} \mathbf{u} - q \partial_{\nu} \mathbf{u} \cdot \boldsymbol{\nu})(\boldsymbol{\nu} \cdot \boldsymbol{\nu}) \\ - \int_{\Gamma_i} \mathbf{v} \cdot \mathbf{g}' + \int_{\Omega} \mathbf{v} \cdot \mathbf{f}' . \end{aligned} \quad (2.46)$$

In the end, we see that

$$D_{\mathcal{V}} \mathcal{J}(\mathbf{u})(\mathcal{V}) = \int_{\Omega} (\mathbf{u} - \mathbf{u}^*) \mathbf{u}' = \int_{\Omega} (-\nu \Delta \mathbf{v} + \nabla q) \cdot \mathbf{u}' \quad (2.47)$$

for all \mathbf{u}' satisfying the boundary conditions of problem (2.41). The above results lead to the adjoint problem for (\mathbf{v}, q)

$$\begin{cases} -\nu \Delta \mathbf{v} + \nabla q = \mathbf{u} - \mathbf{u}^* & \text{in } \Omega \\ \nabla \cdot \mathbf{v} = 0 & \text{in } \Omega \\ \mathbf{v} = \mathbf{0} & \text{on } \Gamma \\ -\nu \partial_{\nu} \mathbf{v} + q \boldsymbol{\nu} = \mathbf{0} & \text{on } \Gamma_i \cup \Gamma_o \end{cases} . \quad (2.48)$$

Therefore,

$$D_{\mathcal{V}} \mathcal{J}(\mathbf{u}, \mathbf{v}, q)(\mathcal{V}) = \int_{\Gamma} (\nu \partial_{\nu} \mathbf{v} \cdot \partial_{\nu} \mathbf{u} - q \partial_{\nu} \mathbf{u} \cdot \boldsymbol{\nu})(\boldsymbol{\nu} \cdot \boldsymbol{\nu}) - \int_{\Gamma_i} \mathbf{v} \cdot \mathbf{g}' + \int_{\Omega} \mathbf{v} \cdot \mathbf{f}' . \quad (2.49)$$

As we mentioned in the previous section, the Hadamard-Zolesio structure theorem [74, 26, 84] implies that there exist $\tilde{\mathbf{g}}$ and $\tilde{\mathbf{f}}$ such that we can write

$$\int_{\Gamma_i} \mathbf{v} \cdot \mathbf{g}' = \int_{\Gamma_i} (\mathbf{v} \cdot \tilde{\mathbf{g}}) (\mathcal{V} \cdot \boldsymbol{\nu}) \quad , \quad \int_{\Omega} \mathbf{v} \cdot \mathbf{f}' = \int_{\partial\Omega} (\mathbf{v} \cdot \tilde{\mathbf{f}}) (\mathcal{V} \cdot \boldsymbol{\nu}) \quad (2.50)$$

and thus (2.49) becomes

$$\left\langle D_{\mathcal{V}} \mathcal{J}, \zeta \right\rangle_{\partial\Omega} = \left\langle \chi_{\Gamma} (\nu \partial_{\nu} \mathbf{v} \cdot \partial_{\nu} \mathbf{u} - q \partial_{\nu} \mathbf{u} \cdot \boldsymbol{\nu}) - \chi_{\Gamma_i} (\mathbf{v} \cdot \tilde{\mathbf{g}}) + \mathbf{v} \cdot \tilde{\mathbf{f}}, \zeta \right\rangle_{\partial\Omega} \quad . \quad (2.51)$$

where χ_D denotes the characteristic function of a domain D . In this section we consider constant forcing terms ($\mathbf{f}' \equiv 0$) and inlet boundary condition ($\mathbf{g}' \equiv 0$) which simplify (2.51) to

$$\boxed{\left\langle D_{\mathcal{V}} \mathcal{J}, \zeta \right\rangle_{\Gamma} = \left\langle \nu \partial_{\nu} \mathbf{v} \cdot \partial_{\nu} \mathbf{u} - q \partial_{\nu} \mathbf{u} \cdot \boldsymbol{\nu}, \zeta \right\rangle_{\Gamma}} \quad . \quad (2.52)$$

For the propagation of the boundary $\partial\Omega$ the same methodology applies as that in part IV of section 2.1.1, albeit for a shape gradient taking the value $\zeta^* = -\nu \partial_{\nu} \mathbf{v} \cdot \partial_{\nu} \mathbf{u} + q \partial_{\nu} \mathbf{u} \cdot \boldsymbol{\nu}$ on Γ . Also, the shape inference algorithm (algorithm 2) applies as is, where one only needs to substitute the solution of the Poisson problem with the Stokes problem.

III Numerics

The numerical methods were already described in part VI of section 2.1.1 for the Poisson problem. Here, we extend these methods for the Stokes problem, following Massing *et al.* [55]. The weak form of the Stokes problem (2.39) reads

$$\int_{\Omega} \nu \nabla \mathbf{v} : \nabla \mathbf{u} + \int_{\Gamma} \mathbf{v} \cdot (-\nu \partial_{\nu} \mathbf{u} + p \boldsymbol{\nu}) - \int_{\Omega} (\nabla \cdot \mathbf{v}) p - \int_{\Omega} q (\nabla \cdot \mathbf{u}) = \int_{\Omega} \mathbf{v} \cdot \mathbf{f} + \int_{\Gamma_i} \mathbf{v} \cdot \mathbf{g} \quad (2.53)$$

which holds for all $\mathbf{v} \in H^1(\Omega) \times H^1(\Omega)$, with \mathbf{v} also vanishing on Γ , and $q \in L^2(\Omega)$. We choose to weakly satisfy the zero-Dirichlet (no-slip) condition on Γ using Nitsche's method, and write

$$\begin{aligned} \int_{\Omega} \nu \nabla \mathbf{v} : \nabla \mathbf{u} + \int_{\Gamma} \mathbf{v} \cdot (-\nu \partial_{\nu} \mathbf{u} + p \boldsymbol{\nu}) - \int_{\Omega} (\nabla \cdot \mathbf{v}) p - \int_{\Omega} q (\nabla \cdot \mathbf{u}) + \mathcal{N}(\mathbf{u}, \mathbf{v}, q, \gamma) \\ = \int_{\Omega} \mathbf{v} \cdot \mathbf{f} + \int_{\Gamma_i} \mathbf{v} \cdot \mathbf{g} \end{aligned} \quad (2.54)$$

where

$$\mathcal{N}(\mathbf{u}, \mathbf{v}, q, \gamma) = \int_{\Gamma} (-\nu \partial_{\nu} \mathbf{v} + q \boldsymbol{\nu}) \cdot (\mathbf{u} - \mathbf{0}) + \frac{\gamma}{h} \mathbf{v} \cdot (\mathbf{u} - \mathbf{0}) \quad (2.55)$$

is the corresponding Nitsche term. The weak form (2.54) now holds for all $\mathbf{v} \in H^1(\Omega) \times H^1(\Omega)$ (\mathbf{v} does not have to vanish on Γ), and $q \in L^2(\Omega)$. Next, we express the problem in the discretized space V_h , defined by (2.31), and let both the velocity components and the pressure be elements

of V_h . As this is known to violate the inf-sup condition¹⁴ [12] for the Stokes problem, leading to an unstable numerical scheme, we include an additional stabilization term, namely $c(\mathbf{u}_h, p_h, q_h)$, to stabilize the pressure¹⁵. The discretized problem then takes the form: find (\mathbf{u}_h, p_h) such that

$$\begin{aligned} a(\mathbf{u}_h, \mathbf{v}_h) + b(\mathbf{u}_h, q_h) + b(\mathbf{v}_h, p_h) \\ + j_u(\mathbf{u}_h, \mathbf{v}_h) + j_p(q_h, p_h) + c(\mathbf{u}_h, p_h, q_h) = i(\mathbf{v}_h, q_h) \end{aligned} \quad (2.56)$$

holds for all $\mathbf{v}_h \in V_h \times V_h$ and $q_h \in V_h$, with

$$a(\mathbf{u}_h, \mathbf{v}_h) := \int_{\Omega} \nu \nabla \mathbf{v}_h : \nabla \mathbf{u}_h + \int_{\Gamma} -\nu (\mathbf{v}_h \cdot \partial_{\nu} \mathbf{u}_h) - \nu (\partial_{\nu} \mathbf{v}_h \cdot \mathbf{u}_h) + \frac{\gamma}{h} (\mathbf{v}_h \cdot \mathbf{u}_h) \quad (2.57a)$$

$$b(\mathbf{u}_h, q_h) := - \int_{\Omega} q_h (\nabla \cdot \mathbf{u}_h) + \int_{\Gamma} (q_h \boldsymbol{\nu}) \cdot \mathbf{u}_h \quad (2.57b)$$

$$j_u(\mathbf{u}_h, \mathbf{v}_h) := \sum_{F \in \mathcal{F}_h^p} \int_F \gamma_1 h [\nabla \mathbf{u}_h][\nabla \mathbf{v}_h] \quad (2.57c)$$

$$j_p(q_h, p_h) := \sum_{F \in \mathcal{F}_h^p} \int_F \gamma_2 h^3 [\nabla p_h][\nabla q_h] \quad (2.57d)$$

$$c(\mathbf{u}_h, p_h, q_h) := - \int_{\Omega} \beta h^2 (-\Delta \mathbf{u}_h + \nabla p_h) : \nabla q_h \quad (2.57e)$$

$$i(\mathbf{v}_h, q_h) := \int_{\Omega} \mathbf{v}_h \cdot \mathbf{f} + \int_{\Gamma_i} \mathbf{v}_h \cdot \mathbf{g} - \int_{\Omega} \beta h^2 (\mathbf{f} \cdot \nabla q_h) \quad (2.57f)$$

We briefly explain the purpose of the above forms. First, a is the discretized Laplacian, supplemented by its boundary conditions, and b describes the coupling between velocity and pressure so that the incompressibility condition is satisfied¹⁶. Thus, a, b and the first two integrals of the functional i , compose the weak form of the Stokes equation for the Nitsche problem, given by (2.54). Then, j_u, j_p are the cut-cell ghost-penalization terms, with the accompanying constants γ_1, γ_2 , for the velocity and the pressure, respectively, discussed in part VI of section 2.1.1. Finally, c and the last integral appearing in i , are the pressure-Poisson stabilization terms, with constant β . Note that $\Delta \mathbf{u}_h \equiv \mathbf{0}$ since we consider bilinear finite elements \mathcal{Q}_1 .

Lastly, we proceed as in part VI of section 2.1.1, to take a basis $\{\varphi_i\}_{i=1}^n$ of V_h and write $\mathbf{u}_h = \sum_{j=1}^n \mathbf{u}_j \varphi_j$, $p_h = \sum_{i=1}^n p_j \varphi_j$, $\mathbf{v}_h = \sum_{i=1}^n \varphi_i$ and $q_h = \sum_{i=1}^n \varphi_i$ to find that the solution of the system

$$\begin{pmatrix} A & B \\ C & D \end{pmatrix} \begin{pmatrix} \mathbf{u} \\ p \end{pmatrix} = \begin{pmatrix} F \\ G \end{pmatrix} \quad (2.58)$$

¹⁴This actually means that the function space where we consider the pressure is richer, i.e. has more degrees of freedom, than it should have. Numerically, this translates to spurious, oscillatory solutions for the pressure.

¹⁵Known as pressure-Poisson stabilized Galerkin method.

¹⁶In fact, the pressure p acts as a Lagrange multiplier to satisfy $\nabla \cdot \mathbf{u} = 0$ in Ω [30].

where

$$\begin{aligned}
A_{ij} &:= a(\varphi_i, \varphi_j) + j_{\mathbf{u}}(\varphi_i, \varphi_j) & B_{ij} &:= b(\varphi_i, \varphi_j) \\
C_{ij} &:= b(\varphi_j, \varphi_i) & D_{ij} &:= j_p(\varphi_i, \varphi_j) + c(\varphi_i, \varphi_j) \\
F_i &:= \langle \varphi_i, \mathbf{f} \rangle_{\Omega} + \langle \varphi_i, \mathbf{g} \rangle_{\Gamma_i} & G_i &:= -\langle \beta h^2 \mathbf{f}, \nabla \varphi_i \rangle_{\Omega}
\end{aligned} \tag{2.59}$$

is a finite dimensional approximation of the problem (2.56). To solve the above system, we use the Schur complement to first solve

$$(CA^{-1}B - D)p = CA^{-1}F - G \tag{2.60}$$

for the pressure p , and then find the velocity \mathbf{u} as the solution of

$$A\mathbf{u} = F - Bp \quad . \tag{2.61}$$

Note that the Schur complement $S := CA^{-1}B - D$ is full, even though A, B, C, D are sparse matrices. Therefore, we use an iterative solver (LGMRES), and work with matrix-vector products, where inversions are replaced by the solution of a (sparse) linear system.

IV Results

We test the Stokes shape inference algorithm for two cases, both corresponding to the two-dimensional flow of a very viscous fluid along a curved channel. In the absence of real MRV data, we generate synthetic data by solving the Stokes problem (2.39) on Ω^* , the ground truth. To generate Ω^* we draw¹⁷ an image I (200×200 pixels) of a geometry that we would like to test (figure 2.6) and use the Chan-Vese image segmentation algorithm [21]¹⁸ to extract its level-set. Then, the level-set is fed to the numerical solver to identify Ω^* and solve the Stokes problem. The initial domain Ω_0 , in the case of the curved channel (figure 2.6a), is defined by the signed distance function

$$(\phi_{\pm})_0 = -0.51 + \sqrt{y^2} \quad , \quad \text{for } x, y \in I \equiv [-1.25, 1.25]^2 \quad . \tag{2.62}$$

For the dummy blood vessel (figure 2.6b), we consider a domain Ω_0 that resembles Ω^* , but is perturbed so that it is visibly narrower before the outlet, compared to Ω^* . The rest of the parameters that we use to launch the shape inference algorithm are outlined in table 2.2 for the curved channel, and table 2.3 for the dummy blood vessel.

For the curved channel, the results are shown in figure 2.7. We observe that for the ideal signal the algorithm reconstructs the ground truth Ω^* in 44 iterations (figures 2.7a, 2.7c) and that the value of the error functional is reduced by almost 7 orders of magnitude during that process. To generate the noisy signal we corrupt the ideal signal by adding Gaussian white noise, resulting in a signal-to-noise ratio ranging from 0 to 50. Now, it takes only about 5

¹⁷We use [Ipe drawing editor](#).

¹⁸We use the implementation provided in scikit-image [80] Python module with default parameters.

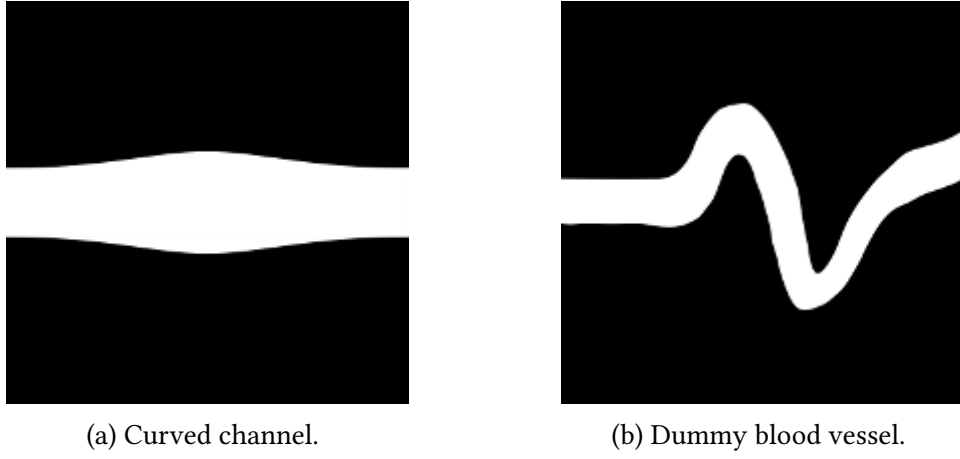


Fig. 2.6 Images used to generate the ground truth domains Ω^* , in which the Stokes problem is solved. We consider flow from left to right, therefore Γ_i, Γ_o are the left and right boundaries of the image, respectively.

Table 2.2 Stokes shape inference algorithm (algorithm 2) parameters for the curved channel.

Model input			Optimization input				Numerics						
ν	\mathbf{f}	\mathbf{g}	ϵ	τ_ζ	$\tau_{i=0}$	ϵ_{tol}	i_{max}	ℓ_{max}	Res. (n)	γ	γ_1	γ_2	β
1.	(0.,0.)	(-2.5·10 ⁴ ,0.)	0.1	15.	0.05	10 ⁻⁶	100	10	200 ² px	10.	1.	0.05	0.2

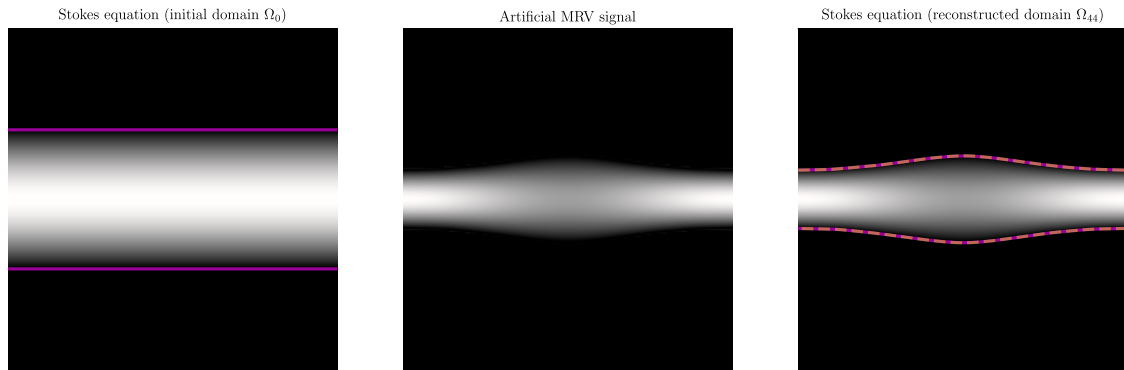
Table 2.3 Stokes shape inference algorithm (algorithm 2) parameters for the dummy blood vessel.

Model input			Optimization input				Numerics						
ν	\mathbf{f}	\mathbf{g}	ϵ	τ_ζ	$\tau_{i=0}$	ϵ_{tol}	i_{max}	ℓ_{max}	Res. (n)	γ	γ_1	γ_2	β
1.	(0.,0.)	(-2.5·10 ⁴ ,0.)	5·10 ⁻³	15.	5·10 ⁻³	10 ⁻⁶	100	10	200 ² px	10.	1.	0.05	0.2

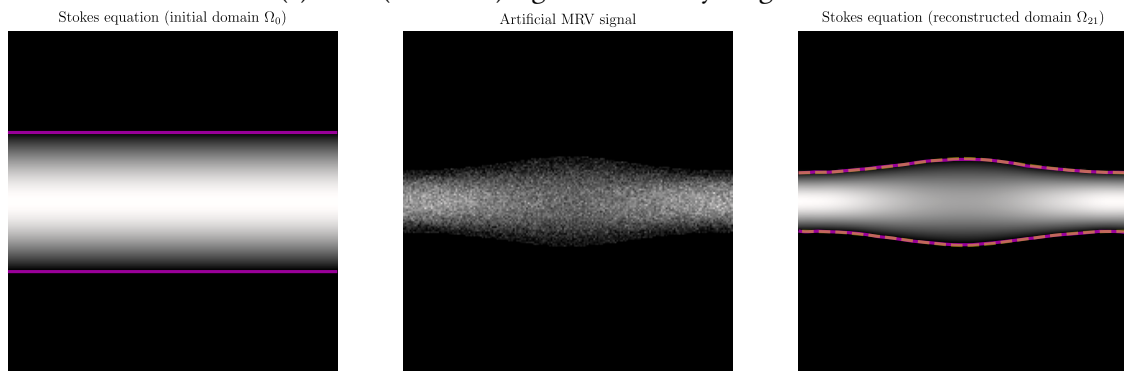
iterations for the algorithm to converge to an error functional value that is reduced by almost 3 orders of magnitude. Nevertheless, the reconstructed domain Ω_{21} approximates Ω^* well (to plotting accuracy). The dummy blood vessel geometry (figure 2.8) presents a more challenging problem involving high-curvature regions. Figures 2.8a,2.8c show that, for the ideal signal, it takes 22 iterations for the algorithm to reconstruct Ω^* , reducing the L^2 -error by more than 2 orders of magnitude. For the noisy signal (SNR ranging from 0 to 80) (figures 2.8b, 2.8d), the error is reduced by almost one order of magnitude in about 10 iterations. As we already mentioned in part VII of section 2.1.1, we anticipate that the reconstruction will be poor near neighbourhoods of Γ where shape perturbations have a minor effect on $\|\mathbf{u} - \mathbf{u}^*\|_{L^2(I)}^2$. For instance, from figures 2.8a, 2.8b we observe that the reconstructed domain deviates from the ground truth near regions¹⁹ where the velocity, and its derivatives, go to zero. Fortunately, this

¹⁹In this case, the outer sides of the two turning points of the dummy blood vessel.

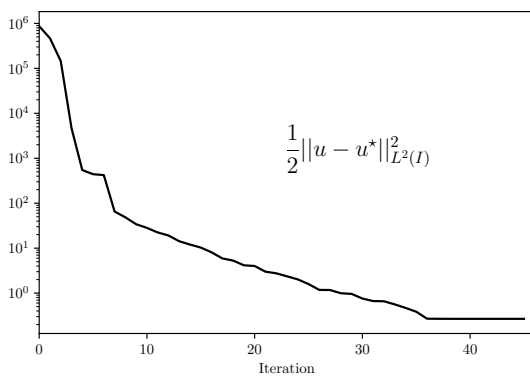
means that the reconstructed shape, although not exact, will exhibit similar velocity fields and velocity gradients²⁰ as the ground truth Ω^* .



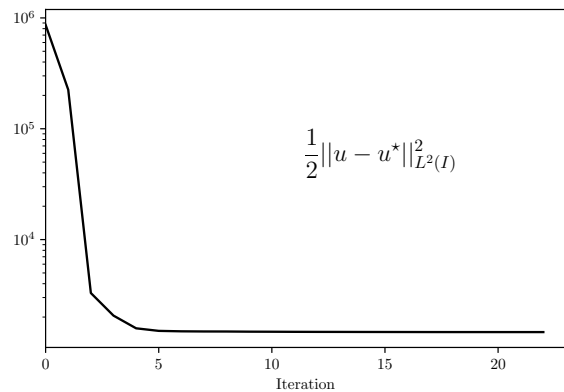
(a) Ideal (noiseless) signal of velocity magnitude.



(b) Noisy signal of velocity magnitude.



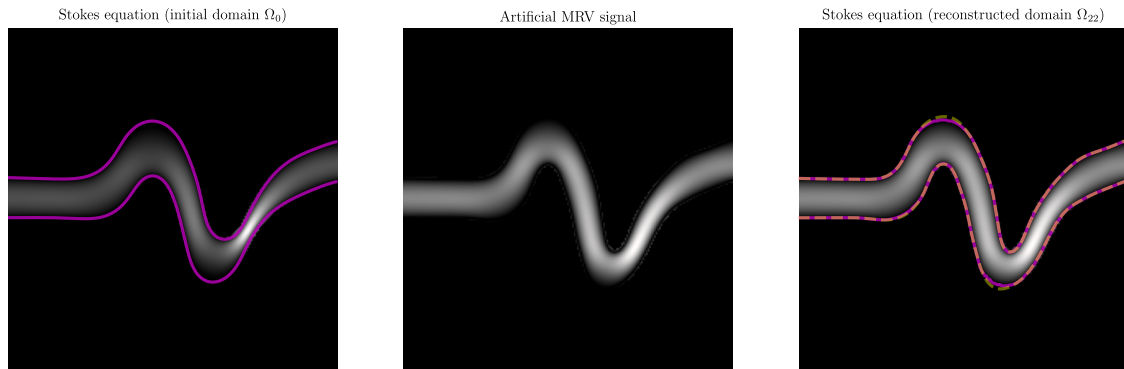
(c) Ideal (noiseless) signal.



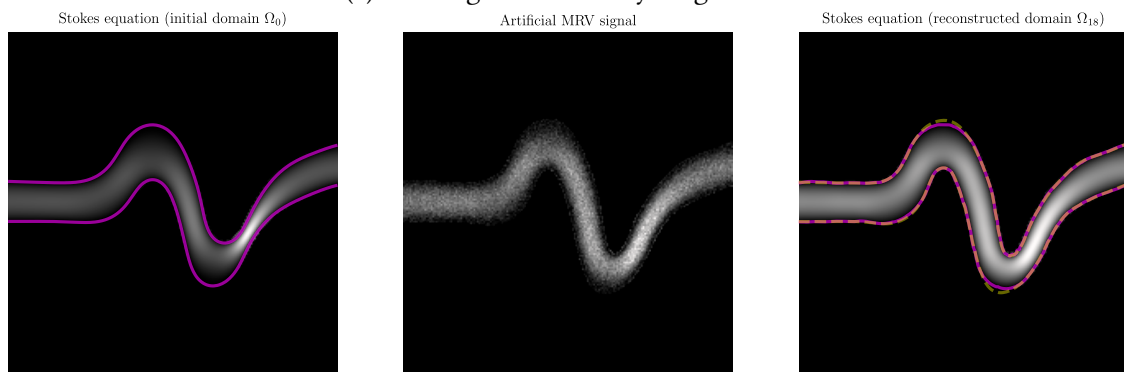
(d) Noisy signal.

Fig. 2.7 Inferring the shape of an object Ω^* (curved channel) from synthetic MRV data, using the Stokes equation (flow is from left to right). The purple line denotes the shape of the reconstructed domain while the yellow dashed line depicts the ground truth (where the lines overlap they seem orange).

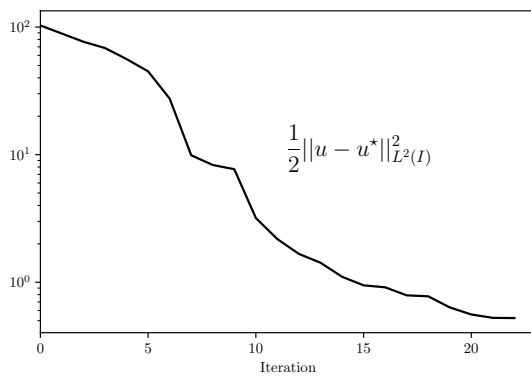
²⁰This also implies that the reconstructed domain will exhibit similar wall-shear stress distributions. Which is important for applications in haemodynamics.



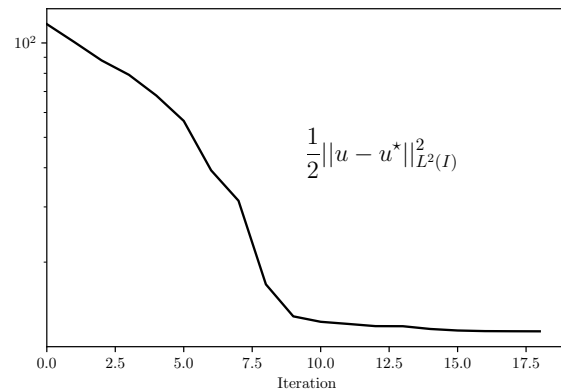
(a) Ideal signal of velocity magnitude.



(b) Noisy signal of velocity magnitude.



(c) Ideal signal.



(d) Noisy signal.

Fig. 2.8 Inferring the shape of an object Ω^* (dummy blood vessel) from synthetic MRV data, using the Stokes equation (flow is from left to right). The purple line denotes the shape of the reconstructed domain while the yellow dashed line depicts the ground truth (where the lines overlap they seem orange).

2.2 Viscosity, forcing and boundary conditions

In section 2.1, we used the Poisson and the Stokes problems to construct the theoretical twin of an MRV experiment. However, these models involve additional unknown parameters, such as the kinematic viscosity ν , the forcing term \mathbf{f} and the inlet Neumann boundary condition \mathbf{g} , in the case of the Stokes problem, for example. Therefore, if these parameters cannot be specified with some degree of certainty, the physical model may not be able to interpret the experimental velocity fields \mathbf{u}^* . In turn, this implies that either the model velocity \mathbf{u} cannot approximate the experimental measurement \mathbf{u}^* , or that matching \mathbf{u} with \mathbf{u}^* will most likely produce a reconstructed domain that does not approximate Ω^* . The above realizations motivate the formulation of a combined optimization problem, where the unknown parameters are included in the reconstruction process, using similar, yet simpler methods than the ones of section 2.1.

2.2.1 Euler-Lagrange equations

To evaluate the sensitivity of the inverse problem to the model parameters, we start by writing the action functional

$$\begin{aligned}
 \mathcal{J}(\mathbf{u}, \mathbf{v}, p, q; \nu, \mathbf{f}, \mathbf{g}) &= \underbrace{\frac{1}{2} \int_I (\mathbf{u} - \mathbf{u}^*)^2}_{\text{flow matching}} \\
 &- \underbrace{\int_{\Omega} \nu \nabla \mathbf{v} : \nabla \mathbf{u} - \int_{\Gamma} \mathbf{v} \cdot (-\nu \partial_{\nu} \mathbf{u} + p \boldsymbol{\nu}) - \int_{\Gamma_i} \mathbf{v} \cdot \mathbf{g} + \int_{\Omega} (\nabla \cdot \mathbf{v}) p + \int_{\Omega} q (\nabla \cdot \mathbf{u}) + \int_{\Omega} \mathbf{v} \cdot \mathbf{f}}_{\text{Stokes equation (weak form)}} \\
 &- \underbrace{\int_{\Gamma} (-\nu \partial_{\nu} \mathbf{v} + q \boldsymbol{\nu}) \cdot (\mathbf{u} - \mathbf{0}) + \frac{\gamma}{h} \mathbf{v} \cdot (\mathbf{u} - \mathbf{0})}_{\text{Nitsche terms for no-slip condition}} = 0
 \end{aligned} \tag{2.63}$$

where \mathbf{v}, q can be seen as the Lagrange multipliers for the velocity and pressure, respectively, used to enforce the constraint that the Nitsche problem for the Stokes equation (2.54) is satisfied. The minimization of the action functional is an optimization problem where one seeks to minimize the discrepancy $\mathbf{u} - \mathbf{u}^*$, in a weak sense, along trajectories characteristic to the Stokes problem. Due to the linearity of the above differential operators, it is easy to see that for $\tau \in \mathbb{R}$

$$\frac{d}{d\tau} \mathcal{J}(\mathbf{u} + \tau \mathbf{u}', \dots) \Big|_{\tau=0} = 0 \quad , \quad \frac{d}{d\tau} \mathcal{J}(\dots, p + \tau p', \dots) \Big|_{\tau=0} = 0 \tag{2.64}$$

are the Euler-Lagrange equations that correspond to the adjoint problem (2.48). Similarly,

$$\frac{d}{d\tau} \mathcal{J}(\dots, \mathbf{v} + \tau \mathbf{v}', \dots) \Big|_{\tau=0} = 0 \quad , \quad \frac{d}{d\tau} \mathcal{J}(\dots, q + \tau q', \dots) \Big|_{\tau=0} = 0 \tag{2.65}$$

correspond to the Nitsche formulation of the Stokes problem (2.39). Next, we compute the first variations of \mathcal{J} with respect to the model parameters $(\nu, \mathbf{f}, \mathbf{g})$. We find

$$\left. \frac{d}{d\tau} \mathcal{J}(\dots, \nu + \tau\nu', \dots) \right|_{\tau=0} = \left\langle \frac{\partial \mathcal{J}}{\partial \nu}, \nu' \right\rangle_{\Omega} = \left\langle -\nabla \mathbf{v} : \nabla \mathbf{u} + \chi_{\Gamma}(\mathbf{v} \cdot \partial_{\nu} \mathbf{u} + \mathbf{u} \cdot \partial_{\nu} \mathbf{v}), \nu' \right\rangle_{\Omega} \quad (2.66a)$$

$$\left. \frac{d}{d\tau} \mathcal{J}(\dots, \mathbf{f} + \tau\mathbf{f}', \dots) \right|_{\tau=0} = \left\langle \frac{\partial \mathcal{J}}{\partial \mathbf{f}}, \mathbf{f}' \right\rangle_{\Omega} = \left\langle \mathbf{v}, \mathbf{f}' \right\rangle_{\Omega} \quad (2.66b)$$

$$\left. \frac{d}{d\tau} \mathcal{J}(\dots, \mathbf{g} + \tau\mathbf{g}', \dots) \right|_{\tau=0} = \left\langle \frac{\partial \mathcal{J}}{\partial \mathbf{g}}, \mathbf{g}' \right\rangle_{\Gamma_i} = \left\langle -\mathbf{v}, \mathbf{g}' \right\rangle_{\Gamma_i} \quad (2.66c)$$

which are the generalized derivatives of the model parameters. The Stokes problem (2.39), its adjoint (2.48), and the first variations (2.66) constitute the Euler-Lagrange equations of the action functional (2.63). Note that ν and ν' are constants, not functions like \mathbf{f} , \mathbf{f}' and \mathbf{g} , \mathbf{g}' . For nonhomogeneous fluids (i.e. spatially-varying ν), such as blood in small blood vessels (less than 100 μm), we need to consider the second order term $\nabla \cdot (\nu \nabla u)$, instead of $\nu \Delta u$, and then repeat the above derivation for (2.66a). However, here we assume that the fluid is Newtonian, with either constant density ρ or constant (dynamic) viscosity μ .

2.2.2 Regularization

More often than not, there are many different sets of parameters $(\nu, \mathbf{f}, \mathbf{g})$, producing solutions u that minimize \mathcal{J} . That is, the optimization problem does not admit a unique solution. For example, it is possible that the solution u is invariant under certain perturbations of the model parameters, or that two parameters have a counteracting effect on u . Numerically, this means that our solution to the optimization problem will be particularly sensitive to the optimization parameters (step-size, initial guess etc.), and difficult to converge.

I Variational techniques

This problem originates from the assumption that \mathbf{f} , \mathbf{g} , for example, are functions in L^2 , i.e. square-integrable. As L^2 is a very rich space of ‘wild’ functions, we would like to restrict \mathbf{f} , \mathbf{g} to a subspace of L^2 , of ‘tameable’ functions: for instance, H^1 , the space of square-integrable functions with square-integrable first derivatives, for which $H^1 \subset L^2$. For any function u to be a member of H^1 , it suffices to show that $\|u\|_{H^1} < \infty$. Therefore, to regularize \mathbf{f} we may add the term

$$\mathcal{R}(\mathbf{f}, \alpha) = \frac{\alpha}{2} \|\mathbf{f} - \mathbf{f}_0\|_{H^1(\Omega)}^2 \quad (2.67)$$

to the action functional (2.63), where $\alpha > 0$ is a weighting constant, and $\mathbf{f}_0 \in (H^1(\Omega))^2$ is the prior knowledge; that is, we expect \mathbf{f} to be close to \mathbf{f}_0 . Taking into account (2.67), (2.66b)

recasts to

$$\begin{aligned} \left\langle \frac{\partial \mathcal{J}}{\partial \mathbf{f}}, \mathbf{f}' \right\rangle_{\Omega} &= \left\langle \mathbf{v} + \alpha(\mathbf{f} - \mathbf{f}_0 - \Delta(\mathbf{f} - \mathbf{f}_0)), \mathbf{f}' \right\rangle_{\Omega} \\ &= \left\langle -\alpha\Delta\mathbf{f} + \alpha\mathbf{f} + (\mathbf{v} - \alpha\mathbf{f}_0 + \alpha\Delta\mathbf{f}_0), \mathbf{f}' \right\rangle_{\Omega} \end{aligned} \quad (2.68)$$

yielding a screened Poisson problem for \mathbf{f} . We could as well consider only the H^1 -seminorm²¹

$$\mathcal{R}(\mathbf{f}, \alpha) = \frac{\alpha}{2} |\mathbf{f} - \mathbf{f}_0|_{H^1(\Omega)}^2 \quad (2.69)$$

and find

$$\left\langle \frac{\partial \mathcal{J}}{\partial \mathbf{f}}, \mathbf{f}' \right\rangle_{\Omega} = \left\langle -\alpha\Delta\mathbf{f} + (\mathbf{v} + \alpha\Delta\mathbf{f}_0), \mathbf{f}' \right\rangle_{\Omega} \quad (2.70)$$

yielding a Poisson problem for \mathbf{f} . The same regularization technique applies to \mathbf{g} . Regularization methods for ill-posed variational inverse problems with applications to image processing are reviewed in [6].

II Gaussian random fields

Interestingly, we can reach appropriate regularization norms \mathcal{R} by formulating a stochastic problem. We briefly explain the process. We first consider a Hilbert space (e.g. L^2) of Gaussian random fields (functions). The Gaussian measure γ has the property that its finite-dimensional projections are multivariate Gaussian distributions, and it is uniquely defined by its mean $m \in L^2$

$$m = \mathbb{E}x = \int_{L^2} x \gamma(dx) \quad (2.71)$$

and its covariance $C : L^2 \times L^2 \rightarrow \mathbb{R}$, for any pair $h, h' \in L^2$

$$C(h, h') = \int_{L^2} \langle h, x \rangle \langle h', x \rangle \gamma(dx) \quad . \quad (2.72)$$

The above (Bochner) integrals define integration over the function space L^2 , under the measure γ . We also define the covariance operator $\mathcal{C} : L^2 \rightarrow L^2$ as

$$\mathcal{C}h = \int_{L^2} x \langle h, x \rangle \gamma(dx) \quad (2.73)$$

and note that $\langle \mathcal{C}h, h' \rangle = C(h, h')$. What we have written above is simply a generalization of Gaussian measures in Hilbert spaces, and fortunately makes sense because the (Bochner) integrals are well defined due to Fernique's theorem²². As we already mentioned in part I of

²¹Under additional assumptions, $|u|_{H^1(\Omega)} < \infty \Rightarrow \|u\|_{H^1(\Omega)} < \infty$ (Poincaré inequality), thus $u \in H^1(\Omega)$.

²²Generalization of the property of Gaussian measures to have 'Gaussian tails' [40].

section 2.2.2, L^2 is a space of ‘wild’ functions. To regularize the problem we restricted our attention to a subspace with smoother functions, H^1 in particular. Now, we will see that the appropriate subspace arises by choosing a covariance operator \mathcal{C} .

As any Gaussian measure in L^2 is uniquely defined by its mean and covariance operator, we write $\gamma = \mathcal{N}(m, \mathcal{C})$. It can be shown that there is a natural Hilbert space H_γ that corresponds to γ and that [10]

$$H_\gamma = \sqrt{\mathcal{C}}(L^2) \quad ,$$

i.e. any function in H_γ belongs to the image of $\sqrt{\mathcal{C}}$. The corresponding inner product

$$\langle h, h' \rangle_\gamma = \langle \mathcal{C}^{-1/2}h, \mathcal{C}^{-1/2}h' \rangle \quad (2.74)$$

defines the norm $\|h\|_\gamma^2$, which is the variance of h . Therefore, the appropriate subspace of L^2 is H_γ , given that we can specify a covariance operator for, e.g. the behaviour of the model parameter \mathbf{f} . This is how prior knowledge is now inserted into our formulation, to mitigate the ill-posedness of the inverse problem. For example, if we take $\mathcal{C} = -\sigma^2 \Delta^{-1}$ ²³, for $\mathbb{R} \ni \sigma > 0$ and consider functions u in Ω such that $u|_{\partial\Omega} = 0$, from (2.74) we find that

$$\langle h, h' \rangle_\gamma = \frac{1}{\sigma^2} \langle \nabla h, \nabla h' \rangle$$

with the inner product generating the H^1 -seminorm, and thus $H_\gamma(\Omega) = H_0^1(\Omega)$. More examples can be found in [76, Chapter 7.21]. This approach, where the appropriate norm \mathcal{R} is implicitly defined through \mathcal{C} by considering randomness in the model parameters, is discussed in [75].

2.2.3 Two problems with multiple unknowns

At the start of section 2.2, we stressed the importance of including additional unknown model parameters in the formulation of the inverse problem. In this section, we present the results of two inverse problems with multiple unknowns. First, we assimilate real MRV data of pipe flow into a Poisson problem, and infer the shape of the pipe Ω^* and the forcing term f . Next, we generate synthetic MRV data of channel flow, and assimilate them into the Stokes problem to infer the shape of the channel Ω^* and the inlet pressure (Neumann) boundary condition.

I Pipe flow: shape and forcing inference

The MRV data u^* (128^2 pixels), in this case, correspond to a real experiment of pipe flow²⁴. An appropriate theoretical twin is the Poisson problem (Poiseuille flow) $-\Delta u = f$ in Ω , with zero Dirichlet boundary condition on $\partial\Omega$. Therefore, we consider both Ω and f to be unknown

²³In general, we can consider the fractional Laplacian operator $-\Delta^s$, for $s > 0$ [51, 50], or a covariance kernel function (e.g. squared exponential) as in machine learning [66].

²⁴Data provided by Andy Sederman, Magnetic Resonance Research Center, University of Cambridge.

model parameters and seek to minimize

$$\mathcal{J} = \frac{1}{2\sigma_u^2} \|u - u^*\|_{L^2(I)}^2 + \frac{1}{2\sigma_f^2} |f - f_0|_{H_0^1(I)} \quad (2.75)$$

where the second term encodes prior information regarding f to mitigate the ill-posedness of the inverse problem, as was discussed in the previous section. Again, we use algorithm 2 and include f in the same line search that we use for ϕ_{\pm} (the domain), and under the same pseudo-timestep²⁵. We start with a domain Ω_0 given by

$$(\phi_{\pm})_0 = -0.5 + \sqrt{x^2 + y^2} \quad , \quad x, y \in I \equiv [-1.25, 1.25]$$

and a constant forcing term $f_0 \equiv 0.1$. The parameters used for this inverse problem are listed in table 2.4.

Table 2.4 Parameters for the inverse problem (Poisson model) (algorithm 2).

Model input		Optimization input				Numerics					
f_0	ϵ	τ_{ζ}	σ_u	σ_f	$\tau_{i=0}$	ε_{tol}	i_{max}	ℓ_{max}	Resolution (n)	γ	γ_1
0.1	0.05	15.0	0.001	10.	0.1	10^{-6}	40	10	256^2 px	10.0	1.0

Figure 2.9 presents the results at two different sections of the pipe. At section 1 (figure 2.9a) we observe a flattened and non-axisymmetric velocity profile, characterising undeveloped flow. For Poiseuille flow, f would correspond to $-\mu^{-1} \partial p / \partial x$, for a pressure gradient $\partial p / \partial x$ that is constant, and the flow would be axisymmetric and developed. As undeveloped flow cannot be described by a Poisson equation, the forcing term f should be considered as a model-error parameter, instead of a quantity with physical meaning²⁶. Even if we cannot assign a physical quantity to f , for this particular problem, we still need it to match the model solution u to the data u^* and to properly reconstruct Ω^* . The results (figures 2.9a, 2.9c) show the reconstruction that is obtained for a value of \mathcal{J} that has been reduced about three orders of magnitude. Note that the velocity maximum, which is located at the upper left quadrant, is properly captured, and associated with a high value of f (figure 2.10a). At section 2 (figure 2.9b) we observe a parabolic distribution of u and axisymmetry, i.e. signs of developed pipe flow. If the flow were ‘ideally developed’ we would expect a constant value of f within Ω_{40} (figure 2.10b). Even if f is far from constant, comparing to the f obtained at section 1 (figure 2.10a), we see that the model-error term of section 1 presents smaller variations and is more uniform. Lastly, as we have no knowledge of the ground truth Ω^* , we cannot judge the accuracy of Ω_{40} (the

²⁵This is very restricting and causes many problems in the optimization. A Newton, or quasi-Newton, algorithm (BFGS in function space) would be a better choice and should be considered in future work.

²⁶Even when the Navier-Stokes equations are used, f is commonly used as a control parameter (most often in data assimilation, and when the focus is primarily on matching the data to the model). This is probably because f is both easy to control and has big (global) impact on the solution. However, when f is not associated with a physical property of the flow, the revised model may not be able to extrapolate (i.e. it is overfitting the data u^*). For instance, a non-zero f could generate turbulence in an otherwise laminar flow.

reconstruction). Nonetheless, we can assert that a general image segmentation algorithm would not have been capable of capturing the precise boundary of the pipe with the same accuracy ²⁷.

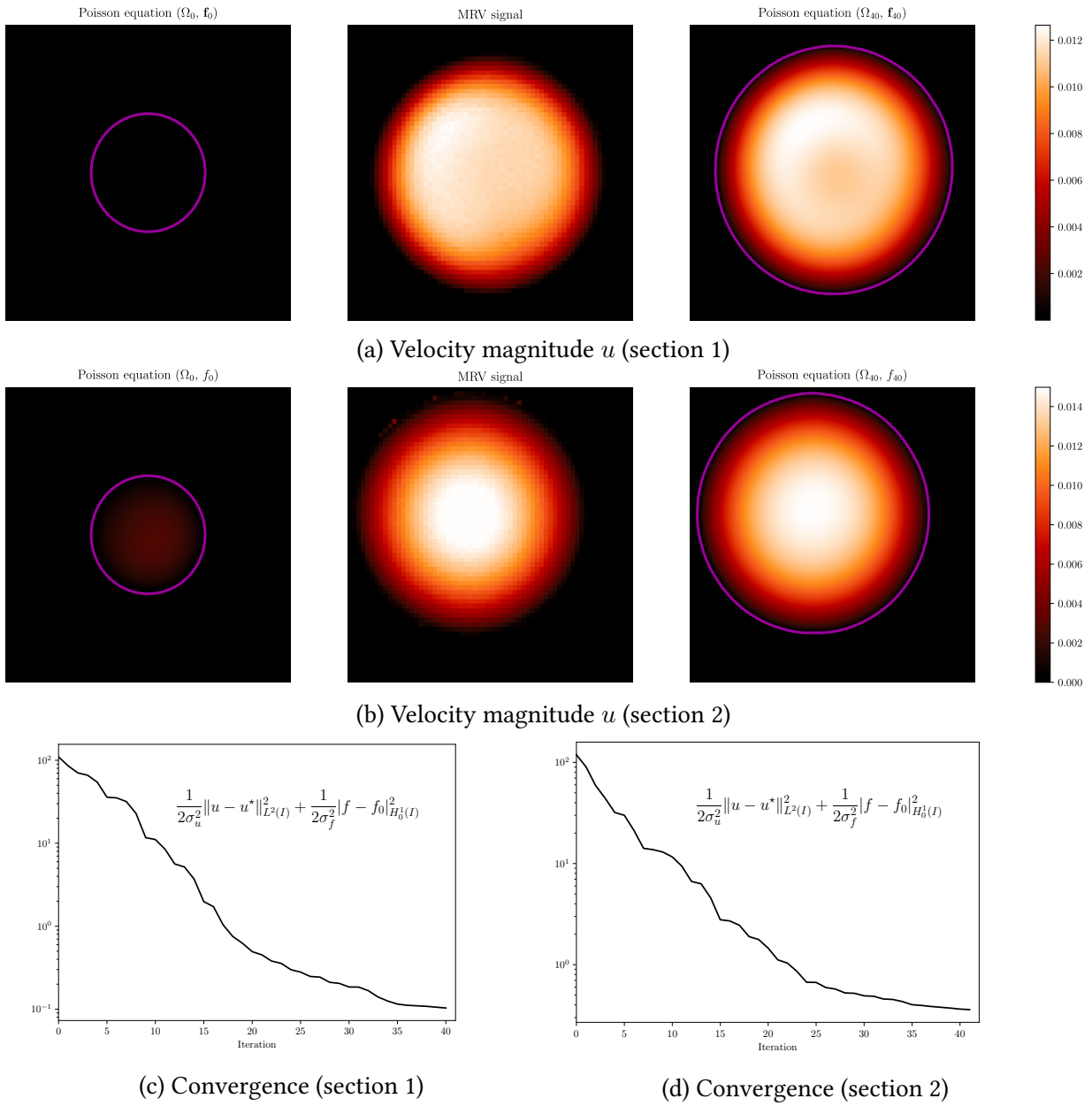


Fig. 2.9 Solution to pipe flow inverse problem at two different sections of the pipe (a,b), and convergence curve for \mathcal{J} (b,c). At section 1 the flow is undeveloped. The purple line denotes the shape of the reconstructed domain.

II Stokes flow in channel: shape and boundary condition inference

We end this section by solving the same problem as that in part IV of section 2.1.2, for the shape inference of a curved channel with synthetic MRV data, but now we treat the inlet boundary

²⁷Assuming that the no-slip condition holds (for hydrophobic coatings/engravings this condition is violated).

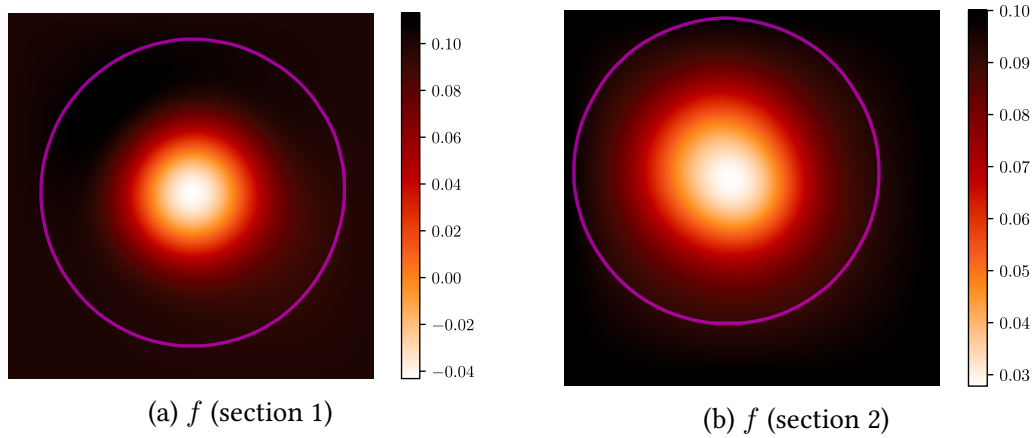


Fig. 2.10 Inferred forcing term f for the pipe flow inverse problem.

condition \mathbf{g} as an unknown. More precisely, we seek Ω and \mathbf{g} that minimize

$$\mathcal{J} = \frac{1}{2\sigma_u^2} \|\mathbf{u} - \mathbf{u}^*\|_{L^2(I)}^2 + \frac{1}{2\sigma_g^2} |g_x - (g_x)_0|$$

where $\mathbf{g} = (g_x, g_y)$ is the Neumann boundary condition at the inlet, with $g_x, g_y \in \mathbb{R}$. The starting domain Ω_0 is given by (2.62), the starting value for \mathbf{g} is $\mathbf{g}_0 = (-15, 0)$, and the ground truth is $\mathbf{g}^* = (-25, 0)$. The rest of the parameters are collected in table 2.5.

Table 2.5 Stokes shape inference algorithm (algorithm 2) parameters for the curved channel.

Model input		Optimization input				Numerics								
ν	\mathbf{f}	ϵ	τ_ζ	σ_u	σ_g	$\tau_{i=0}$	ϵ_{tol}	i_{max}	ℓ_{max}	Res. (n)	γ	γ_1	γ_2	β
1.	(0.,0.)	0.1	15.	1.	100.	0.05	10^{-6}	100	10	200 ² px	10.	1.	0.05	0.2

Figure 2.11 sums up the results and the convergence history of this problem. We observe that both Ω and \mathbf{g} are properly reconstructed, compared to the ground truth, and that small errors are attributed to the bad convergence properties of the optimization algorithm (steepest descent). Also, note that during the very first iteration g_x decreases in magnitude (figure 2.11b), getting further away from the ground truth. This is because the velocity magnitude u is higher than u^* in the starting domain Ω_0 , so g_x starts increasing in magnitude only after a substantial change in Ω has occurred. This interplay between the unknown parameters can cause major problems when a naive optimization algorithm is used. Therefore, we stress again that a more sophisticated Newton, or quasi-Newton (as in [88, 34]), algorithm has to be considered in future applications (properly extended to function spaces), in order to improve both the convergence rate and the accuracy.

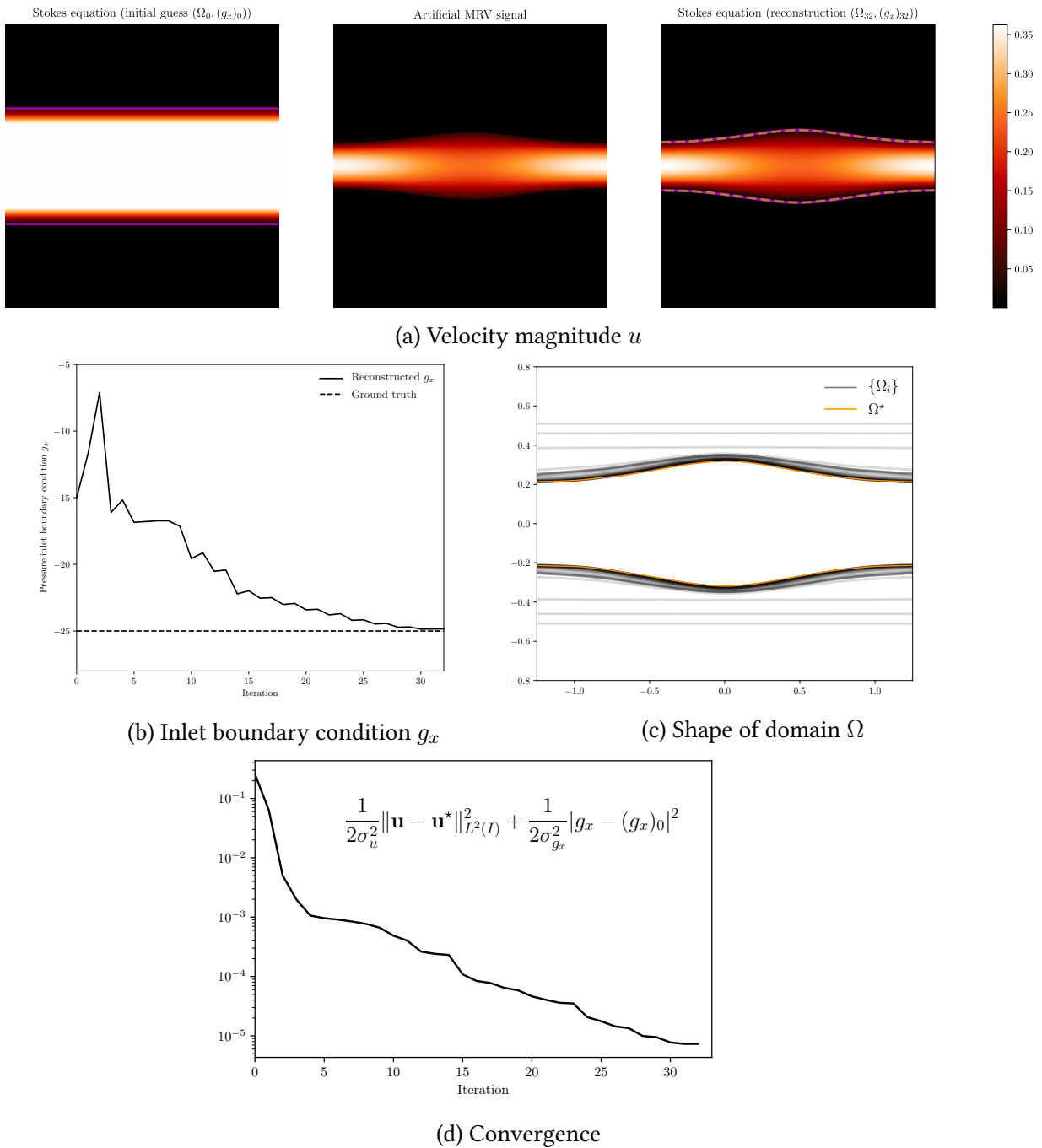


Fig. 2.11 Solution to channel flow inverse problem for synthetic MRV data. The purple line denotes the reconstructed domain while the yellow line depicts the ground truth (where the lines overlap they seem orange). Darker color in (c) is due to lines overlapping, visualizing the convergence rate of the sequence $\{\Omega_i\}$.

Chapter 3

Conclusions and future work

I Conclusions

We have developed a prototype method to infer the shape of blood vessel boundaries from magnetic resonance velocimetry data. The method relies on (inverse) shape optimization techniques and is formulated in a natural framework for problems with moving domains. In particular, we implicitly define the boundaries in terms of signed distance functions and use Nitsche's method to weakly enforce the Dirichlet boundary condition on the moving front. The moving of the domain is expressed by an advection-diffusion equation for the signed distance function, which allows for topological changes. Then, we introduce additional unknown model parameters to the inverse problem, such as the kinematic viscosity ν , the forcing term \mathbf{f} and the inlet boundary condition \mathbf{g} . We provide two alternative perspectives about the type of the regularization \mathcal{R} one should choose : i) a purely variational perspective in function spaces, and ii) an approach based on Gaussian measures and random functions. However, the choice of \mathcal{R} still depends on the nature of the a priori knowledge. Finally, we test the methods for the Poisson and the Stokes problems using both real and synthetic (artificial) MRV measurements. The extension of the above methods to the Navier-Stokes problem is under development.

II Future work

To achieve the research objectives, we prioritize the following tasks:

1. Extension of the previously discussed methods to the Navier-Stokes problem in \mathbb{R}^2 .

We aim to test the above methods using the Navier-Stokes problem as the theoretical twin of a real MRV experiment. After discussions with Andy Sederman and Scott Elgersma from the Magnetic Resonance Research Center of University of Cambridge, the first experiments will involve two-dimensional axisymmetric flow in simple arrangements ¹.

2. Extension to the Navier-Stokes problem in \mathbb{R}^3 for steady and periodic flows.

¹These will involve tapered tubes.

The extension to \mathbb{R}^3 is necessary in order to formulate proper inverse problems with applications in haemodynamics. In general, the geometry of large blood vessels does not allow for two-dimensional approximations. As the extension in \mathbb{R}^3 brings considerable implementational effort and increased computational cost, we may have to consider more sophisticated software such as the [deal.ii](#) library [1]. At this moment, all of the methods discussed herein, are implemented by the author using Python and its scientific computing libraries on a laptop.

3. Assimilating MRV data directly from \mathbf{k} -space.

So far we have considered discrepancy norms of the type

$$\mathcal{J} = \|\mathbf{u} - \mathbf{u}^*\|_{L^2(I)}$$

where \mathbf{u}, \mathbf{u}^* are in physical space. If the frequency space is densely sampled there is no need for reconstruction; we simply take $\mathbf{u}^* = \mathcal{F}^{-1}\hat{\mathbf{u}}^*$. However, to reduce signal acquisition times we usually undersample the \mathbf{k} -space. For undersampled signals $\mathcal{F}^{-1}\hat{\mathbf{u}}^*$ will most probably be contaminated with noise or artefacts. Therefore, instead of assimilating $\mathcal{F}^{-1}\hat{\mathbf{u}}^*$ it may be more natural to consider assimilating the data directly in \mathbf{k} -space by taking the norm

$$\|\hat{\mathbf{u}}^* - \mathcal{S}\mathcal{F}\mathbf{u}\|_{L^2} \quad .$$

We believe that this approach has not been considered before due to the difficulties of solving boundary value problems in complex geometries using spectral methods. If the theoretical twin remains in the physical space, a possible approach would be to flip the problem and define the norm as

$$\|\mathcal{F}^{-1}\mathcal{S}^{-1}\hat{\mathbf{u}}^* - \mathbf{u}\|_{L^2(I)} \quad .$$

However, this brings us back to \mathcal{J} , except if $\hat{\mathbf{u}}^*$ is extended using $\hat{\mathbf{u}}$ and then then projected on the full \mathbf{k} -space by \mathcal{S}^{-1} , in order to compensate for the artefacts and noise.

Another approach would be to formulate the problem on a wavelet basis [25]. In 1988, Daubechies [24] showed how to construct an orthonormal basis of compactly supported wavelets in $L^2(\mathbb{R})$. This discovery had a considerable impact in mathematics and physics, since it implied that any function in $L^2(\mathbb{R})$ can be expressed in terms of such a basis². What differentiates wavelets from classic harmonic analysis, is that they have local support in both the physical and frequency spaces, with the localization at each space depending on the uncertainty principle³. They are also characterized by optimal (information) compression, multiresolution and adaptivity⁴. The main difficulty for the solution of boundary value problems lies on the rather complicated methods for their construction, and the definition of the boundary conditions. Still, wavelets have found many applications in fluid dynamics and turbulence [70, 44]. For example,

²Therefore, since we are mainly working in L^2 , all of the methods that we have previously discussed (except the numerics) immediately apply to Daubechie's wavelets.

³In contrast, a Fourier transform provides absolute knowledge of frequency and zero spatial information.

⁴It is worth noting that the [JPEG2000](#) image compression protocol is among the state-of-the-art methods and the coding standard of digital cinema.

we mention the construction of divergence-free wavelets, studied in [27, 11, 49], and the use of wavelets for fictitious domain methods [48, 5], similar to the one used in the present study. Lastly, wavelets have also been used in magnetic resonance imaging [65, 39].

4. Extension of the optimization algorithm to Newton or quasi-Newton.

As we previously mentioned, the steepest descent algorithm that we use can be very inefficient. We aim to extend the algorithm to a Newton, or quasi-Newton (BFGS-like) algorithm. This will also allow us to study confidence intervals (or uncertainties) around the critical point.

5. Magnetic resonance velocimetry experiments.

We are collaborating with Andy Sederman and Scott Elgersma, from the Magnetic Resonance Research Center of University of Cambridge, to design experiments and apply the above methods.

References

- [1] Arndt, D., Bangerth, W., Blais, B., Clevenger, T. C., Fehling, M., Grayver, A. V., Heister, T., Heltai, L., Kronbichler, M., Maier, M., Munch, P., Pelteret, J.-P., Rastak, R., Thomas, I., Turcksin, B., Wang, Z., and Wells, D. (2020). The deal.II library, version 9.2. *Journal of Numerical Mathematics*.
- [2] Atabek, H. B. (1968). Wave Propagation through a Viscous Fluid Contained in a Tethered, Initially Stressed, Orthotropic Elastic Tube. *Biophysical Journal*, 8(5):626–649.
- [3] Atabek, H. B. and Ling, S. C. (1972). A nonlinear analysis of pulsatile flow in arteries. *Journal of Fluid Mechanics*, 55:493–511.
- [4] Babuška, I., Banerjee, U., and Osborn, J. E. (2003). Survey of meshless and generalized finite element methods: A unified approach. *Acta Numerica*, 12(2003):1–125.
- [5] Baccou, J. and Liandrat, J. (2005). On coupling wavelets with fictitious domain approaches. *Applied Mathematics Letters*, 18(12):1325–1331.
- [6] Benning, M. and Burger, M. (2018). Modern regularization methods for inverse problems. *Acta Numerica*, 27:1–111.
- [7] Benning, M., Gladden, L., Holland, D., Schönlieb, C. B., and Valkonen, T. (2014). Phase reconstruction from velocity-encoded MRI measurements - A survey of sparsity-promoting variational approaches. *Journal of Magnetic Resonance*, 238:26–43.
- [8] Bessems, D., Rutten, M., and Van De Vosse, F. (2007). A wave propagation model of blood flow in large vessels using an approximate velocity profile function. *Journal of Fluid Mechanics*, 580:145–168.
- [9] Blythe, T. W., Sederman, A. J., Mitchell, J., Stitt, E. H., York, A. P., and Gladden, L. F. (2015). Characterising the rheology of non-Newtonian fluids using PFG-NMR and cumulant analysis. *Journal of Magnetic Resonance*, 255:122–131.
- [10] Bogachev, V. I. (1998). *Gaussian measures*. American Mathematical Society.
- [11] Bostan, E., Unser, M., and Ward, J. P. (2015). Divergence-free wavelet frames. *IEEE Signal Processing Letters*, 22(8):1142–1146.
- [12] Brenner, Susanne, Scott, R. (2008). *The Mathematical theory of finite element methods*, volume 15. Texts in Applied Mathematics, Springer.
- [13] Burger, M. (2001). A level set method for inverse problems. *Inverse Problems*, 17(5):1327–1355.
- [14] Burger, M. (2003). A framework for the construction of level set methods for shape optimization and reconstruction. *Interfaces and Free Boundaries*, 5(3):301–329.
- [15] Burger, M. and Osher, S. J. (2005). A Survey in Mathematics for Industry: A survey on level set methods for inverse problems and optimal design. *European Journal of Applied Mathematics*, 16(2):263–301.

- [16] Burman, E. (2010). La pénalisation fantôme. *Comptes Rendus Mathématique*, 348(21-22):1217–1220.
- [17] Burman, E. and Hansbo, P. (2012). Fictitious domain finite element methods using cut elements: II. A stabilized Nitsche method. *Applied Numerical Mathematics*, 62(4):328–341.
- [18] Callaghan, P. (2001). *Principles of nuclear magnetic resonance microscopy*. Clarendon Press, Oxford University Press.
- [19] Callaghan, P. T. (2013). *Translational Dynamics and Magnetic Resonance*. Oxford University Press.
- [20] Candès, E. J., Romberg, J., and Tao, T. (2006). Robust Uncertainty Principles : Exact Signal Frequency Information. *IEEE Transactions on Information Theory*, 52(2):489–509.
- [21] Chan, T. F. and Vese, L. A. (2001). Active contours without edges. *IEEE Transactions on Image Processing*, 10(2):266–277.
- [22] Cotter, S. L., Dashti, M., Robinson, J. C., and Stuart, A. M. (2009). Bayesian inverse problems for functions and applications to fluid mechanics. *Inverse Problems*, 25(11).
- [23] Crane, K., Weischedel, C., and Wardetzky, M. (2017). The heat method for distance computation. *Communications of the ACM*, 60(11):90–99.
- [24] Daubechies, I. (1988). Orthonormal bases of compactly supported wavelets. *Communications on Pure and Applied Mathematics*, 41(7):909–996.
- [25] Daubechies, I. (1992). *Ten Lectures on Wavelets*. CBMS-NSF Regional Conference Series in Applied Mathematics.
- [26] Delfour, M. and Zolesio, J.-P. (2011). *Shapes and Geometries: Analysis, Differential Calculus, and Optimization*. 2nd ed., Advances in Design and Control 22, SIAM, Philadelphia, PA.
- [27] Deriaz, E. and Perrier, V. (2006). Divergence-free and curl-free wavelets in two dimensions and three dimensions: Application to turbulent flows. *Journal of Turbulence*, 7:1–37.
- [28] Donoho, D. L. (2006). Compressed sensing. *IEEE Transactions on Information Theory*, 52(4):1289–1306.
- [29] Duclaux, V., Gallaire, F., and Clanet, C. (2010). A fluid mechanical view on abdominal aortic aneurysms. *Journal of Fluid Mechanics*, 664:5–32.
- [30] Evans, L. C. (2010). *Partial Differential Equations*. American Mathematical Society, second edition.
- [31] Evertz, L. Q., Rassi, E. M., Kennedy, J. R., Codd, S. L., and Seymour, J. D. (2012). Oscillatory Flow Phenomena in Simple and Complex Fluids. *Applied Magnetic Resonance*, 42(2):211–225.
- [32] Fogelson, A. L. and Neeves, K. B. (2015). Fluid mechanics of blood clot formation. *Annual Review of Fluid Mechanics*, 47:377–403.
- [33] Fukushima, E. (1999). Nuclear magnetic resonance as a tool to study flow. *Annual Review of Fluid Mechanics*, 31:95–123.
- [34] Funke, S. W., Nordaas, M., Evju, Ø., Alnæs, M. S., and Mardal, K. A. (2019). Variational data assimilation for transient blood flow simulations: Cerebral aneurysms as an illustrative example. *International Journal for Numerical Methods in Biomedical Engineering*, 35(1):1–27.
- [35] Gillissen, J. J. J., Bouffanais, R., and Yue, D. K. P. (2019). Data assimilation method to de-noise and de-filter particle image velocimetry data. *Journal of Fluid Mechanics*, 877:196–213.

- [36] Gladden, L. F. and Sederman, A. J. (2017). Magnetic Resonance Imaging and Velocity Mapping in Chemical Engineering Applications. *Annual Review of Chemical and Biomolecular Engineering*, 8(1):227–247.
- [37] Gopalakrishnan, S. S., Pier, B., and Biesheuvel, A. (2014). Dynamics of pulsatile flow through model abdominal aortic aneurysms. *Journal of Fluid Mechanics*, 758:150–179.
- [38] Griffith, M. D., Leweke, T., Thompson, M. C., and Hourigan, K. (2009). Pulsatile flow in stenotic geometries: Flow behaviour and stability. *Journal of Fluid Mechanics*, 622:291–320.
- [39] Guerquin-Kern, M., Haberlin, M., Pruessmann, K. P., and Unser, M. (2011). A fast wavelet-based reconstruction method for magnetic resonance imaging. *IEEE Transactions on Medical Imaging*, 30(9):1649–1660.
- [40] Hairer, M. (2009). An Introduction to Stochastic PDEs. Lecture Notes.
- [41] Hoang, V. H., Law, K. J., and Stuart, A. M. (2014). Determining white noise forcing from eulerian observations in the navier-stokes equation. *Stochastics and Partial Differential Equations: Analysis and Computations*, 2(2):233–261.
- [42] Juntunen, M. and Stenberg, R. (2009). Nitsche’s method for general boundary conditions. *Mathematics of Computation*, 78(267):1353–1374.
- [43] Katritsis, D., Kaiktsis, L., Chaniotis, A., Pantos, J., Efstathopoulos, E. P., and Marmarelis, V. (2007). Wall Shear Stress: Theoretical Considerations and Methods of Measurement. *Progress in Cardiovascular Diseases*, 49(5):307–329.
- [44] Kim, T., Thürey, N., James, D., and Gross, M. (2008). Wavelet turbulence for fluid simulation. *SIGGRAPH’08: International Conference on Computer Graphics and Interactive Techniques, ACM SIGGRAPH 2008 Papers 2008*.
- [45] Koltukluoğlu, T. S. (2019). Fourier Spectral Dynamic Data Assimilation : Interlacing CFD with 4D Flow MRI. Technical report, Research Report No. 2019-56, ETH Zurich.
- [46] Koltukluoğlu, T. S., Cvijetić, G., and Hiptmair, R. (2019). Harmonic balance techniques in cardiovascular fluid mechanics. In *Medical Image Computing and Computer Assisted Intervention – MICCAI 2019*, pages 486–494, Cham. Springer International Publishing.
- [47] Koltukluoğlu, T. S. and Blanco, P. J. (2018). Boundary control in computational haemodynamics. *Journal of Fluid Mechanics*, 847:329–364.
- [48] Kunoth, A. (2001). Wavelet techniques for the Fictitious-Domain-Lagrange-Multiplier-Approach. *Numerical Algorithms*, 27(3):291–316.
- [49] Lessig, C. (2019). Divergence Free Polar Wavelets for the Analysis and Representation of Fluid Flows. *Journal of Mathematical Fluid Mechanics*, 21(1):1–8.
- [50] Lischke, A., Pang, G., Gulian, M., Song, F., Glusa, C., Zheng, X., Mao, Z., Cai, W., Meerschaert, M. M., Ainsworth, M., and Karniadakis, G. E. (2020). What is the fractional Laplacian? A comparative review with new results. *Journal of Computational Physics*, 404:109009.
- [51] Lodhia, A., Sheffield, S., Sun, X., and Watson, S. S. (2016). Fractional gaussian fields: A survey. *Probability Surveys*, 13(2016):1–56.
- [52] Lustig, M., Donoho, D., and Pauly, J. M. (2007). Sparse MRI: The application of compressed sensing for rapid MR imaging. *Magnetic Resonance in Medicine*, 58(6):1182–1195.
- [53] Markl, M., Frydrychowicz, A., Kozerke, S., Hope, M., and Wieben, O. (2012). 4D flow MRI. *Journal of Magnetic Resonance Imaging*, 36(5):1015–1036.

- [54] Massing, A., Larson, M. G., and Logg, A. (2013). Efficient implementation of finite element methods on nonmatching and overlapping meshes in three dimensions. *SIAM Journal on Scientific Computing*, 35(1).
- [55] Massing, A., Larson, M. G., Logg, A., and Rognes, M. E. (2014). A Stabilized Nitsche Fictitious Domain Method for the Stokes Problem. *Journal of Scientific Computing*, 61(3):604–628.
- [56] Mirtich, B. (1996). Fast and Accurate Computation of Polyhedral Mass Properties. *Journal of Graphics Tools*, 1(2):31–50.
- [57] Mons, V., Chassaing, J. C., and Sagaut, P. (2017). Optimal sensor placement for variational data assimilation of unsteady flows past a rotationally oscillating cylinder. *Journal of Fluid Mechanics*, 823:230–277.
- [58] Morris, P. D., Narracott, A., Von Tengg-Kobligk, H., Soto, D. A. S., Hsiao, S., Lungu, A., Evans, P., Bressloff, N. W., Lawford, P. V., Rodney Hose, D., and Gunn, J. P. (2016). Computational fluid dynamics modelling in cardiovascular medicine. *Heart*, 102(1):18–28.
- [59] Nerem, R. M., Seed, W. A., and Wood, N. B. (1972). An experimental study of the velocity distribution and transition to turbulence in the aorta. *Journal of Fluid Mechanics*, 52(1):137–160.
- [60] Newling, B., Poirier, C. C., Zhi, Y., Rioux, J. A., Coristine, A. J., Roach, D., and Balcom, B. J. (2004). Velocity imaging of highly turbulent gas flow. *Physical Review Letters*, 93(15):1–4.
- [61] Nitsche, J. (1971). Über ein Variationsprinzip zur Lösung von Dirichlet-Problemen bei Verwendung von Teilräumen, die keinen Randbedingungen unterworfen sind. *Abhandlungen aus dem Mathematischen Seminar der Universität Hamburg*, 36(1):9–15.
- [62] Norris, J. R. (1997). Heat kernel asymptotics and the distance function in Lipschitz Riemannian manifolds. *Acta Mathematica*, 179(1):79–103.
- [63] Osher, S. and Sethian, J. A. (1988). Fronts propagating with curvature-dependent speed: Algorithms based on Hamilton-Jacobi formulations. *Journal of Computational Physics*, 79(1):12–49.
- [64] Pedley, T. J. (1980). *The Fluid Mechanics of Large Blood Vessels*. Cambridge University Press.
- [65] Peters, R. D. and Wood, M. L. (1996). Multilevel wavelet-transform encoding in MRI. *Journal of Magnetic Resonance Imaging*, 6(3):529–540.
- [66] Ramussen, C. E. and Williams, C. K. I. (2006). *Gaussian processes for machine learning*. The MIT Press.
- [67] Rudin, L. I., Osher, S., and Fatemi, E. (1992). Nonlinear total variation based noise removal algorithms. *Physica D: Nonlinear Phenomena*, 60(1-4):259–268.
- [68] Sankaran, S., Kim, H. J., Choi, G., and Taylor, C. A. (2016). Uncertainty quantification in coronary blood flow simulations: Impact of geometry, boundary conditions and blood viscosity. *Journal of Biomechanics*, 49(12):2540–2547.
- [69] Schmoderer, T., Aviles-Rivero, A. I., Corona, V., Debroux, N., and Schönlieb, C.-B. (2020). Learning Optical Flow for Fast MRI Reconstruction. pages 1–28.
- [70] Schneider, K. and Vasilyev, O. V. (2010). Wavelet Methods in Computational Fluid Dynamics. In *Annual Review of Fluid Mechanics*, volume 42, pages 473–503.

- [71] Sethian, J. A. (1996). A fast marching level set method for monotonically advancing fronts. *Proceedings of the National Academy of Sciences of the United States of America*, 93(4):1591–1595.
- [72] Sethian, J. A. and Adalsteinsson, D. (1999). The fast construction of extension velocities in level set methods. *Journal of Computational Physics*, 148:2–22.
- [73] Singer, J. R. (1959). Blood flow rates by nuclear magnetic resonance measurements. *Science*, 130(3389):1652–1653.
- [74] Sokolowski, J. and Zolesio, J.-P. (1992). *Introduction to Shape Optimization*. Springer Series in Computational Mathematics, Springer-Verlag, Berlin, Germany.
- [75] Stuart, A. M. (2010). Inverse problems: A Bayesian perspective. *Acta Numerica*, 19(2010):451–459.
- [76] Tarantola, A. (2005). *Inverse Problem Theory and Methods for Model Parameter Estimation*. SIAM.
- [77] Taylor, C. A. and Figueroa, C. A. (2009). Patient-specific modeling of cardiovascular mechanics. *Annual Review of Biomedical Engineering*, 11:109–134.
- [78] Van De Meent, J. W., Sederman, A. J., Gladden, L. F., and Goldstein, R. E. (2010). Measurement of cytoplasmic streaming in single plant cells by magnetic resonance velocimetry. *Journal of Fluid Mechanics*, 642:5–14.
- [79] Van De Vosse, F. N. and Stergiopoulos, N. (2011). Pulse wave propagation in the arterial tree. *Annual Review of Fluid Mechanics*, 43:467–499.
- [80] Van Der Walt, S., Schönberger, J. L., Nunez-Iglesias, J., Boulogne, F., Warner, J. D., Yager, N., Gouillart, E., and Yu, T. (2014). Scikit-image: Image processing in python. *PeerJ*, 2014(1).
- [81] Varadhan, S. R. (1967a). Diffusion processes in a small time interval. *Communications on Pure and Applied Mathematics*, 20(4):659–685.
- [82] Varadhan, S. R. (1967b). On the behavior of the fundamental solution of the heat equation with variable coefficients. *Communications on Pure and Applied Mathematics*, 20(2):431–455.
- [83] Verma, S., Papadimitriou, C., Lüthen, N., Arampatzis, G., and Koumoutsakos, P. (2019). Optimal sensor placement for artificial swimmers. *Journal of Fluid Mechanics*, 884.
- [84] Walker, S. W. (2015). *The Shapes Of Things: A Practical Guide To Differential Geometry And The Shape Derivative*. Advances in Design and Control, SIAM, Philadelphia, PA.
- [85] Whitmore, R. L. (1968). *Rheology of the circulation*. Pergamon Press, Oxford.
- [86] Womersley, J. (1955). Method for the calculation of velocity, rate of flow and viscous drag in arteries when the pressure gradient is known. *The Journal of Physiology*, 127:553–563.
- [87] Womersley, J. (1957). An elastic tube theory of pulse transmission and oscillatory flow in mammalian arteries. *Wright Air Development Center, WADC Technical Report TR 56-614*.
- [88] Yan, L., James Li, C., and Huang, T. Y. (1996). Function space BFGS quasi-Newton learning algorithm for time-varying recurrent neural networks. *Journal of Dynamic Systems, Measurement and Control, Transactions of the ASME*, 118(1):132–138.
- [89] Yu, H., Juniper, M. P., and Magri, L. (2019). Combined state and parameter estimation in level-set methods. *Journal of Computational Physics*, 399:108950.
- [90] Zhu, C., Seo, J. H., and Mittal, R. (2018). Computational modelling and analysis of haemodynamics in a simple model of aortic stenosis. *Journal of Fluid Mechanics*, 851:23–49.

Appendix A

Shape sensitivity analysis

I Speed fields and the shape derivative

We need a framework to formulate a perturbed boundary value problem with respect to a deforming domain $\Omega \Subset \mathbb{R}^n$. We start by introducing an artificial ‘speed field’ $\mathcal{V} \in \mathcal{D}(\mathbb{R}^n)^n$. Given a speed field \mathcal{V} , and for $\tau \in [0, \epsilon]$ with $\epsilon > 0$, we define $T_\tau(\Omega)(\mathcal{V}) : \Omega \rightarrow \Omega_\tau$ to be the perturbation-of-identity mapping

$$x \mapsto x + \tau \mathcal{V}(x) \quad \text{for every } x \in \Omega \quad . \quad (\text{A.1})$$

For sufficiently small τ , T_τ is a diffeomorphism that maps Ω onto Ω_τ . We also consider \mathcal{O} to be the family of every possible perturbed domain Ω_τ and the mapping $\mathcal{J} : \mathcal{O} \rightarrow \mathcal{D}'(\mathbb{R}^n)$ that takes domains and gives back functionals. Subsequently, given a domain $\Omega \in \mathcal{O}$, $\mathcal{J}(\Omega) : \mathcal{D}(\mathbb{R}^n) \rightarrow \mathbb{R}$ is a functional defined in Ω . The shape (or Gateaux) derivative of the functional $\mathcal{J}(\Omega)$ is defined as

$$D_{\mathcal{V}} \mathcal{J}(\Omega)(\mathcal{V}) := \left. \frac{d}{d\tau} (\mathcal{J}(\Omega_\tau)) \right|_{\tau=0^+} = \lim_{\tau \rightarrow 0} \frac{\mathcal{J}(\Omega_\tau) - \mathcal{J}(\Omega)}{\tau} \quad (\text{A.2})$$

where the limit is to be understood in the topology of \mathcal{D}' .

Realizing that speed fields \mathcal{V} producing nontrivial transformations $T_\tau(\Omega)(\mathcal{V})$ must: i) be supported on $\partial\Omega$ and ii) not be tangential on every point of $\partial\Omega$, we reach a theorem that says that the shape derivative of a functional defined on Ω can be reduced to a functional defined only on its boundary $\partial\Omega$ (Hadamard-Zolesio structure theorem [74, 26]). That is, there exists \tilde{g} such that

$$D_{\mathcal{V}} \mathcal{J}(\Omega)(\mathcal{V}) = \int_{\partial\Omega} \tilde{g}(\mathcal{V} \cdot \boldsymbol{\nu}) \quad . \quad (\text{A.3})$$

II Formulas for the shape derivatives of functionals

Let $u_\tau : \Omega_\tau \rightarrow \mathbb{R}$ be a function in $C^k(\Omega_\tau)$ that depends smoothly on the parameter $\tau \in [0, \epsilon]$ and $u_0 \equiv u$. The material derivative of u with respect to the transformation T_τ is defined as

$$D_{\mathcal{V}}u(x) := \lim_{\tau \rightarrow 0} \frac{(u_\tau \circ T_\tau)(x) - u(x)}{\tau}, \quad x \in \Omega \quad (\text{A.4})$$

A more useful and explicit form is

$$D_{\mathcal{V}}u(x) = u'(x) + (\mathcal{V}(x) \cdot \nabla)u(x) \quad (\text{1.5})$$

where $u' \equiv \partial_\tau u(x)$ is the instantaneous shape derivative of u . Considering the distributed and the boundary functionals \mathcal{E} and \mathcal{J} respectively, defined by

$$\mathcal{E}_\tau = \int_{\Omega_\tau} u_\tau(x) \quad , \quad \mathcal{J}_\tau = \int_{\Gamma_\tau} u_\tau(x) \quad \text{for all } x \in \Omega_\tau, \tau \in [0, \epsilon] \quad (\text{1.6})$$

where $\Gamma_\tau \equiv \partial\Omega_\tau$, the shape derivatives of \mathcal{E} , \mathcal{J} with respect to the transformation $T_\tau(\Omega)(\mathcal{V})$ are

$$D_{\mathcal{V}}\mathcal{E} := \frac{d}{d\tau}\mathcal{E}_\epsilon \Big|_{\tau=0} = \int_{\Omega} u' + \int_{\Gamma} u (\mathcal{V} \cdot \boldsymbol{\nu}) \quad (\text{1.7a})$$

$$D_{\mathcal{V}}\mathcal{J} := \frac{d}{d\tau}\mathcal{J}_\epsilon \Big|_{\tau=0} = \int_{\Gamma} u' + (\partial_\nu u + \kappa u) (\mathcal{V} \cdot \boldsymbol{\nu}) \quad (\text{1.7b})$$

where κ is the mean curvature of Γ . Also, Γ is considered a closed surface, i.e. $\partial\Gamma = \emptyset$. To derive the shape derivative of the functional (1.7a), we first transform it in the reference domain Ω as

$$\mathcal{E}_\tau = \int_{\Omega_\tau} u_\tau(y) dy = \int_{\Omega} (u_\tau \circ T_\tau)(x) \det(\nabla T_\tau) dx \quad .$$

Differentiating with respect to pseudotime τ , we obtain

$$\begin{aligned} \frac{d}{d\tau} \left(\int_{\Omega_\tau} u_\tau(y) dy \right) \Big|_{\tau=0} &= \frac{d}{d\tau} \left(\int_{\Omega} (u_\tau \circ T_\tau)(x) \det(\nabla T_\tau) dx \right) \Big|_{\tau=0} \\ &= \int_{\Omega} D_{\mathcal{V}}u(x) + u(x) \frac{d}{d\tau} \det(\nabla T_\tau) dx \\ &= \int_{\Omega} u'(x) + (\mathcal{V}(x) \cdot \nabla)u(x) + u(x) (\nabla \cdot \mathcal{V}(x)) dx \\ &= \int_{\Omega} u'(x) + \nabla \cdot (\mathcal{V}(x)u(x)) dx \end{aligned}$$

where we have used the formulas $\frac{d}{d\tau} \det(\nabla T_\tau) = \nabla \cdot \mathcal{V}$ and $D_{\mathcal{V}}u = u' + (\mathcal{V}(x) \cdot \nabla)u(x)$. Finally, using the divergence theorem we obtain

$$D_{\mathcal{V}}\mathcal{E}(\Omega)(\mathcal{V}) = \int_{\Omega} u' + \int_{\Gamma} u (\mathcal{V} \cdot \boldsymbol{\nu})$$

To prove (1.7b), first note that [74, Sec. 2.17]

$$\int_{\Gamma_\tau} u_\tau(y) \, dy = \int_{\Gamma_\tau} (u_\tau \circ T_\tau)(x) \, \gamma_\tau \, dx$$

where $\gamma_\tau = \det(\nabla T_\tau) \|(\nabla T_\tau^\top)^{-1} \cdot \boldsymbol{\nu}\|_{\mathbb{R}^n}$ and

$$\gamma'_\tau := \frac{d}{d\tau} \gamma_\tau \Big|_{\tau=0} = \nabla_\Gamma \cdot \mathcal{V} \quad (1.8)$$

where $\nabla_\Gamma := \boldsymbol{\tau} \cdot \nabla$ denotes the tangential derivative and $\boldsymbol{\tau}$ the unit tangential vector. Also [84, Sec. 4.4]

$$\int_\Gamma \nabla_\Gamma \cdot u = \int_\Gamma \kappa u \cdot \boldsymbol{\nu} \quad \text{for any } u \in C^k(\Gamma, \mathbb{R}^n) \quad . \quad (1.9)$$

Using the above formulas, and working as before, we find

$$\begin{aligned} \frac{d}{d\tau} \left(\int_{\Gamma_\tau} u_\tau(y) \, dy \right) \Big|_{\tau=0} &= \frac{d}{d\tau} \left(\int_\Gamma (u_\tau \circ T_\tau)(x) \, \gamma_\tau \, dx \right) \Big|_{\tau=0} \\ &= \int_\Gamma D_{\mathcal{V}} u(x) + u(x) \frac{d}{d\tau} \gamma_\tau \, dx \\ &= \int_\Gamma u'(x) + (\mathcal{V}(x) \cdot \nabla) u(x) + u(x) \nabla_\Gamma \cdot \mathcal{V}(x) \, dx \\ &= \int_\Gamma u'(x) + (\mathcal{V} \cdot \boldsymbol{\nu})(\boldsymbol{\nu} \cdot \nabla) u(x) + (\mathcal{V}(x) \cdot \boldsymbol{\tau}) \nabla_\Gamma u(x) + u(x) \nabla_\Gamma \cdot \mathcal{V}(x) \, dx \\ &= \int_\Gamma u'(x) + (\mathcal{V} \cdot \boldsymbol{\nu}) \partial_{\boldsymbol{\nu}} u(x) + \nabla_\Gamma \cdot (u(x) \mathcal{V}(x)) \, dx \end{aligned}$$

where in the last two lines we decomposed the term $(\mathcal{V}(x) \cdot \nabla) u(x)$ in normal and tangential components. Finally, using formula (1.9) one obtains

$$D_{\mathcal{V}} \mathcal{J}(\Gamma)(\mathcal{V}) = \int_\Gamma u' + (\partial_{\boldsymbol{\nu}} u + \kappa u) (\mathcal{V} \cdot \boldsymbol{\nu}) \quad .$$

